Mapping In-situ Morphological Phase Transitions of Magnetic Domains in $[\mathrm{Co/Pt}]_N$ Multilayers

Michael Vaka

A senior thesis submitted to the faculty of
Brigham Young University
in partial fulfillment of the requirements for the degree of

Bachelor of Science

Dr. Karine Chesnel, Advisor

Department of Physics and Astronomy

Brigham Young University

December 2022

ABSTRACT

Mapping In-situ Morphological Phase Transitions of Magnetic Domains in $[Co/Pt]_N$ Multilayers

Michael Vaka
Department of Physics and Astronomy, BYU
Bachelor of Science

Nanomagnetism is a growing field with many applications from bio-medicine to high-density magnetic storage. Co/Pt multilayers display ferromagnetic domains with perpendicular magnetic anisotropy with distinct morphologies that may be used in magnetic data storage devices. The morphology of the magnetic domains in $[Co/Pt]_N$ multilayer thin films is characterized by types of patterns, such as bubble, stripe, and maze. Previous studies at remanence show that these patterns depend on the number of bilayer repeats, N, the Co thickness, and magnitude of the previously applied field. The domain density is a key metric for quantifying transitions between these morphological phases. To gain insight into these morphological processes, we map the domain density as a response to the in-situ field, H, and maximum applied field, H_m, using Magnetic Force Microscopy (MFM) up to an applied in-situ field of 7.2 kOe. We also mapped characteristics extracted from the Fourier transforms of the MFM images. We completed these studies for $[Co(t),Pt(7\text{ Å})]_{20}$ with $t = 31$ Å and 10 Å. For the first time, we discover three in-situ morphological transitions that correlate to previously observed remanent morphological phases and we find that domain density generally increase with in-situ applied field.

Keywords: Nanomagnetism, Multilayers, In-situ Magnetic Field

ACKNOWLEDGMENTS

I would like to thank Dr. Karine Chesnel for providing this opportunity and mentoring me through the challenges that come with scientific inquiry. This project would not be possible without the endeavors of current and previous students: Aaron Gentillon, Kira Johnson, John(Joey) Ray, Hailey McGhie, Carson Richards, and a special thanks to BYU's College of Physical and Mathematical Science department and the Multicultural Student Services for providing funding for this research and for scholarships funding my education. I would also like to thank my family and friends for the support that they offered me.

Contents

List of Figures

Chapter 1

Introduction

1.1 Magnetism in Materials

Magnetism, in materials, can be studied at the following scales: atomic (Å), microscopic (nm to μm) and macroscopic (sub mm and beyond). Magnetic materials may exhibit various magnetic ordering including paramagnetism, ferromagnetism, ferrimagnetism, diamagnetism, etc. Ordering refers to the symmetries and correlations in a many-particle system. For this study, we are interested in materials that display ferromagnetic or antiferromagnetic ordering because that can be used in nanotechnologies due to their strong magnetization and hysteresis. Magnetic hysteresis is a non-linear process where the ascending and descending branches of the magnetization loop do not line-up.

In this thesis we study $[\mathrm{Co}(t), \mathrm{Pt}(7\ \text{Å})]_{\mathrm{N}}$ multilayers where the parenthesized quantities are the thickness of each layer and N indicates the number of bilayer repeats. Specifically, we study the cases of t = 31 Å and 10 Å. Cobalt is one of the elements that displays the greatest atomic magnetic moments while platinum is non-magnetic yet magnetically permeable. The role of platinum is to space the ferromagnetic layers and introduce shape anisotropy in the out-of-plane direction. This symmetry breaking leads to fascinating behaviors that are not observed in bulk Co crystals, such as the formation of nanoscale magnetic domains. We will explore these phenomena in the chapters that follow.

1.1.1 Technological Application of Nanomagnetism

In the past, magnetic domain patterns in ferromagnetic films had practical applications in magnetic recording devices such as magnetic tape memory and hard disk drives. In more recent years,various applications, such as race-track memory, for nanomagnetic domains are being found [1].

In hard disk drives, there are three important elements: the read head, the write head, and the recording medium. The read head is composed of a tunnel-junction magneto-restive sensor which allows for the effective reading of magnetic fields through a current. The write head is composed of an electromagnetic part and a material that is limited to produced fields of 25 kOe which is generally sufficient to flip domains on the recording media. The recording media is a disk made of ferromagnetic layers where nanoscale magnetic domains would typically form. These disk can rotate up to 15,000 rpm leading to excellent data transfer rates. The advent of solid state memory using micro-transistors has largely dealt a killing blow to this technology [2]

One novel application of magnetic domains in ferromagnetic layers is in bio-inspired computing via spintronics. Bio-inspired computing hopes to replicate computational behaviors of biological systems such as neural pathways found in the brain. Artificial neural networks are one such application of bio-inspired computing found in traditional computers. In contrast, spintronics could replicate neural networks due to the nonlinear dynamics that nanomagnetic systems exhibit which are similar to processes found in neural pathways. But in order to use such systems the information must be stored and transported via a magnetic medium. Bubble magnetic domains such as those found in the samples we study could fulfill this role [3].

1.1.2 Magnetism of Ferromagnetic Materials

The magnetization, M, of a material is a macroscopic quantity of interest and represents the sum of all spins carried by all the atoms in that material at a given time. The magnetic response to the application of a magnetic field leads to hysteresis loops as illustrated in Fig. 1.1. Another magnetic behavior observed in ferromagnetic multilayers is the preference in the magnetization direction, an easy-axis, which is referred to as anisotropy [4]. Next, we discuss magnetization and magnetic anisotropy in the chapter that follows.

In ferromagnetic materials, the magnetic moments tend to line up in a certain direction leading to large magnetization, M, at the macroscopic scale of the material, either bulk or thin film. The magnetic field at which the maximum magnetization is reached is called the saturation field, H_s.

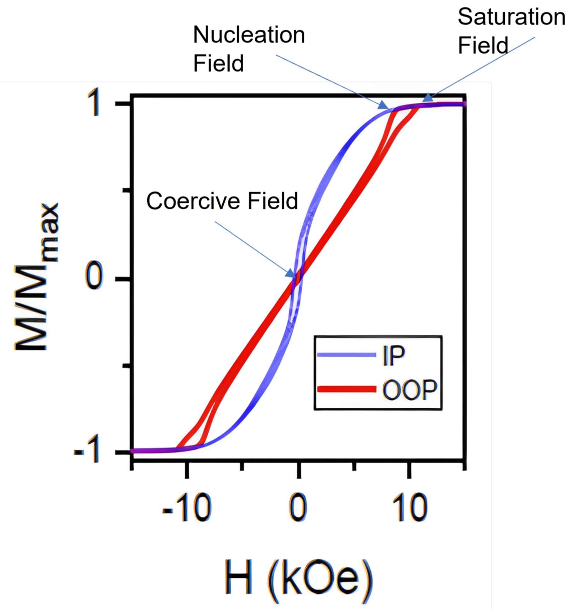

Figure 1.1 Hysteresis loops measured on a [Co(31Å)/Pt(7Å)] thin film via vibrating sample magnetometry (VSM) for two applied field directions – in-plane (IP) and out-of-plane (OOP) with respect to the sample surface. The vertical axis displays the normalized magnetization, M/M_{max}, as a response to applied field. This figure was extracted from [5].

Magnetometry provides a way to probe the macroscopic net magnetization M, as a response to applied field H, which is demonstrated in Fig. 1.1: the plotted curves are measurement loops typically transversed counter-clockwise. In each of these loops we have an ascending branch followed by a descending branch connected by a plateauing region which is where saturation of the sample is achieved. H_s is measured to be when this plateauing first begins. In contrast, the field at which the magnetization leaves the plateau is called the nucleation field. At the origin, we see in the in-plane loop that field is non-zero when there is no-magnetization. The field that brings the magnetization back to zero is called the coercive field. We can interpret the saturation field as indicating when all the magnetic moments align, the nucleation field as indicating – after saturation– when the magnetic moments begin to unalign, and the coercive field as indicating when all the magnetic moments come into a stable equilibrium (no net magnetization) after saturation. These loops may go up to their saturation field (and beyond), in which case they are called a major loop, or to some field below the saturation field, in which case they are called a minor loop.

In ferromagnetic materials there exists sub-volumes of aligned moments called magnetic domains. These magnetic domains form due to energy minimization processes. In ferromagnetic materials, the domains form arbitrarily or form due to defects as seen in Fig. 1.2.

1.1.3 Multilayers and Anisotropy

Certain atoms carry a magnetic moment composed of two parts: the orbital and spin magnetic moment. The orbital moment can be understood from the classical viewpoint as a magnetic moment due to a current produced by the moving point charges around the nucleus. From the quantum perspective, the orbital magnetic moment arises from the angular momentum of the electrons around the nucleus. The spin magnetic moment arises from the intrinsic spin angular momentum of the electron. In a crystal, the orbital magnetic moments are associated with the crystal's axes and lead to the formation of larger magnetization effects such as dipolar interactions.

Ferromagnetic thin-films, when thick enough, generally tend to have in-plane anisotropy. How-

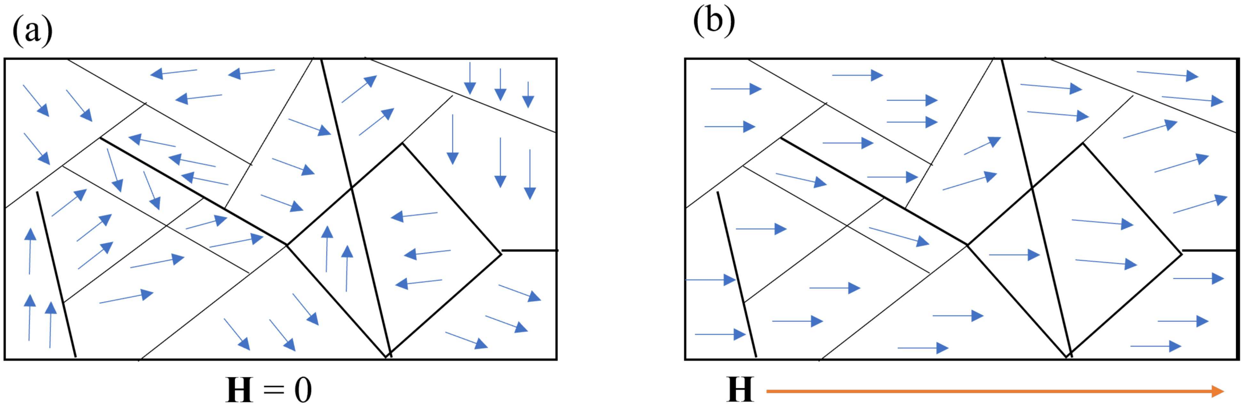

Figure 1.2 Schematics of magnetic domain formation in ferromagnetic materials. In a) there is arbitrary alignment of domains (blue arrows represent local magnetization) typical of ferromagnetic material without net magnetization. In b) the magnetization in all the domains aligns with the applied magnetic field which causes domains to eventually disappear.

ever, as thickness decreases, ferromagnetic thin-films may exhibit anisotropy out-of-plane which is called perpendicular magnetic anisotropy (PMA) [4]. PMA is driven by interfacial effects between layers, which can be described by energy contributions related to the dipolar interactions and the spin-orbital couplings [4].

For Co/Pt multilayers, see Fig. 1.3, the magnetic domains are observed on the surface of the sample. The magnetic domains extend down into the sample with aligned magnetization between Co layers.

1.1.4 Morphology

We study the morphology of two-dimensional patterns which lead to a variety of topologies. In biology the study of morphology refers to the study of shapes and arrangement of parts of organisms and in mathematics it refers to a theory and technique for processing geometrical structures. Similarly, for magnetic materials, the morphology refers to the shape and geometrical structures

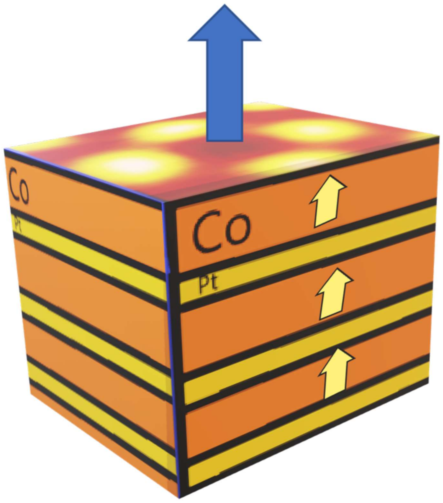

Figure 1.3 Sketch of multilayers for [Co(t)/Pt(7 Å)]$_N$ bi-layers showing a bubble-like magnetic pattern at the surface. The blue arrow indicates perpendicular anisotropy and the yellow arrows indicate magnetization in the sample throughout the thickness of the film.

that the domain pattern exhibits. Some of the morphologies we have observed in Co/Pt multilayers are shown in Fig. 1.4. The bubble states correspond to higher applied fields while the others, stripe, short-stripe, maze, are associated with lower applied fields.

1.2 Previous Research

From previous studies done by Westover et. al. [6], Chesnel et. al. [5], and Fallarino et. al. [7] it was found that domain density is optimized for multilayers [Co(31Å),Pt(7Å)]$_N$ for N = 18 or 20. In the results section, we compare our remanent domain density to the one published in [7].

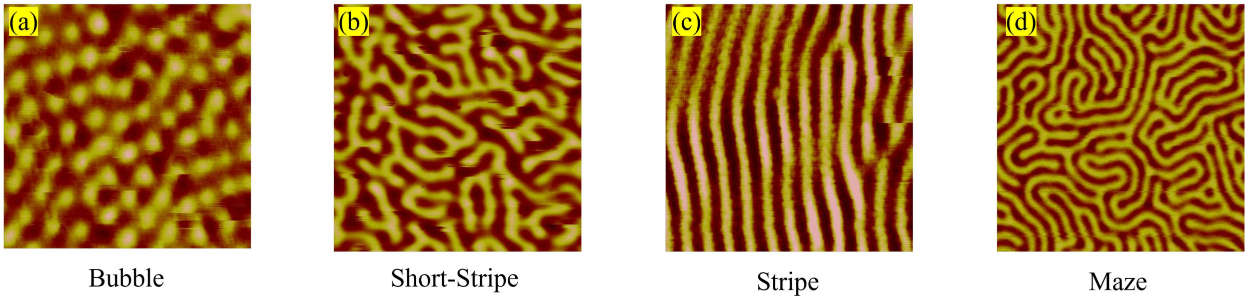

Bubble Short-Stripe Stripe Maze

Figure 1.4 MFM images of 2×2 μm^2 images of [Co(31 Å)/Pt(7 Å)]$_{20}$ showing various magnetic domain morphologies. a) Bubble pattern characterized by circular domains (disks or dots). b) Short-stripe pattern showing striped state domains that visibly end. c) Aligned stripe pattern where domains extend beyond the field of view. d) Maze pattern where domains meander without ending within the field of view.

Chapter 2

Methods

2.1 Experimental Design and Setup

Experimental methods to extract nanomagnetic information from a material include the standard method of magnetometry as well as advanced techniques such as X-ray magnetic circular dichroism and muon scattering. Magnetic force microscopy (MFM) is used here to investigate nanomagnetic information in the real space. MFM captures the force of stray magnetic fields produced by a sample and extract it from the topography of the sample. This is done by scanning the surface of the sample at two heights and subtracting the resulting signals from each other to separate short-range forces and long-range forces.

2.1.1 AFM and MFM

Atomic force microscopy (AFM) captures the topography of a material. It does this by measuring the deflection of a cantilever as it moves across a sample as illustrated in Fig. 2.1. The cantilever is coated with a thin magnetic layer, typically a few nanometers thick, made of a nickel based alloy. There are three operating modes that AFM works in: tapping, contact, and noncontact [8]. In the tapping mode the cantilever oscillates at a frequency right below its resonant frequency and then captures the topography via the changes in amplitude measured by a laser as illustrated in Fig. 2.1

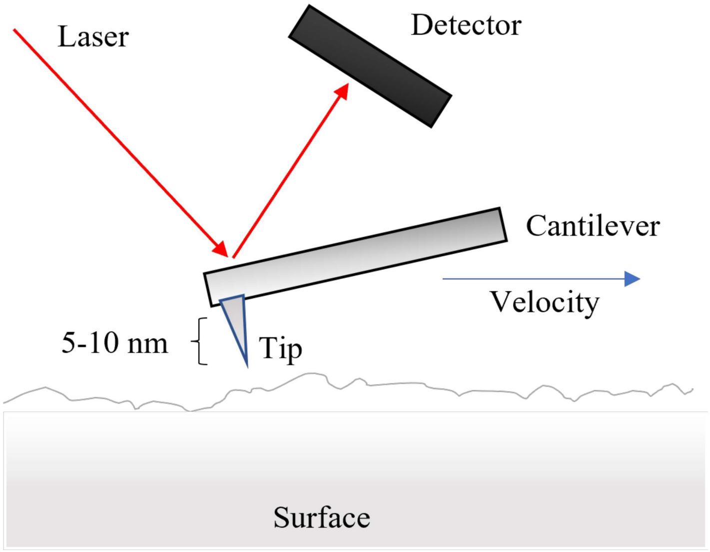

Figure 2.1 Sketch illustrating the principal components of an atomic force microscope. The tip height ranges from 5 to 10 nm while the cantilever has typical thickness of 500 μm with length of 5 mm.

MFM uses the topographical information recorded via AFM and retraces the surface of the sample at some preset height (typically between 20 and 100 nm) above the sample as illustrated in Fig. 2.2. The phase shift of the retrace can be linked to the magnetic forces that are being produced by the sample locally.

The signal is optimized during the AFM scan using several feedback and control parameters: amplitude setpoint, drive amplitude, integral gain, proportional gain, and scan rate. These parameters play an important role in resolving the topography and later the magnetic signal via MFM. These parameters are to be updated when the setup changes or if the signal quality degrades.

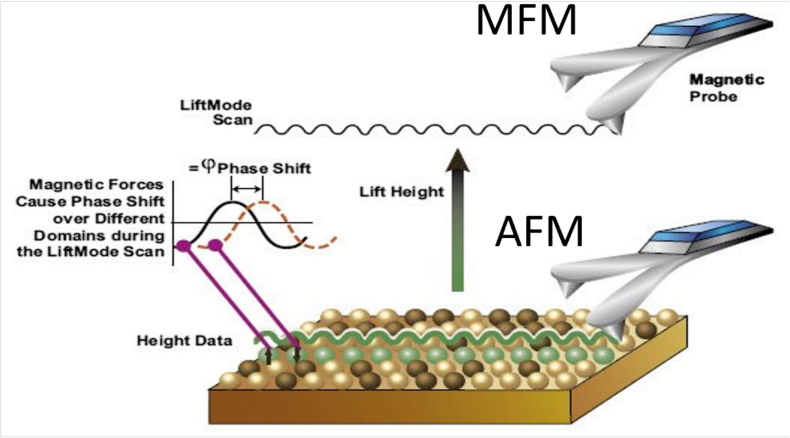

Figure 2.2 Comparative sketch illustrating both magnetic force microscopy (MFM) and atomic force microscopy (AFM) [9].

2.1.2 Experimental Setup

We used the Veeco NanoScope Dimension3100 and NanoScope V to carry out the atomic force microscopy. We captured the response of $[\mathrm{Co/Pt}]_{\mathrm{N}}$ to an in-situ magnetic field, by using permanent magnets and a z-stage to vary the field via the distance separation between the sample and magnets. The experimental setup for the field in-situ setup went through three iterations to optimize the applied field strength and the reproducibility of the magnetic field and data was collected throughout each iteration. The first iteration was composed of a glass slide, Z-stage and a magnet stack. However, the attractive force between the magnet stack and the microscope head would bend the Z-stage base causing uncertainty in the field measurements. In the second iteration, a thicker Z-stage base was machined to resolve the previous issue and proved effective but reduced the range of the applied magnetic field. In the third iteration, a metal block was mounted onto the XY-stage to increase the height of the glass slide. The glass slides were machined to hold the probe in place and reduce the thickness where the sample would be placed which allowed for higher fields and greater reproducibility. This last setup is illustrated in Fig. 2.3. In all these iterations, the glass slide was held in place by three permanent magnets and a free block on the other hand to support the slide and reduce vibrations. We recorded the applied magnetic field as a function of distance from sample using a Gaussmeter from LakeView.

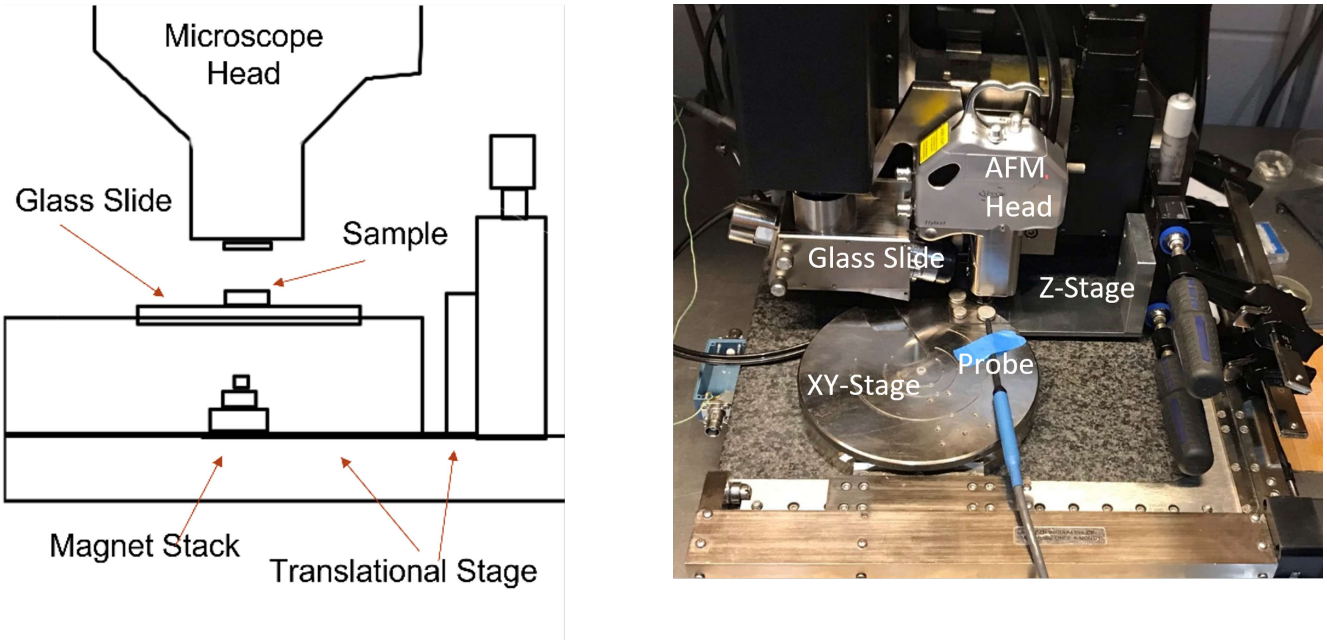

Figure 2.3 Left: Diagram of the experimental setup from behind the XY-stage. Right: Picture of experimental setup from the front.

2.1.3 Experimental Procedure and Validation

The in-situ field measurement procedure is composed of two steps: 1) field calibration and 2) MFM image capture. For the field calibration, we recorded the applied magnetic field at a series of specific heights on the Z-stage typically using field intervals of 0.2 kOe. For the field calibration, we averaged the magnetic field measured over several measurements (accounting for fluctuations), as illustrated in Fig. 2.4.The experimental uncertainty on the field value remains under ±0.5 kOe in the whole field range (it is about ±0.35 kOe at H = 8 kOe, about 0.51 kOe at H = 2.8 kOe and about ± 0.24 kOe at H = 0.93 kOe). Based on these results we conclude the setup is quite robust and reproducible.

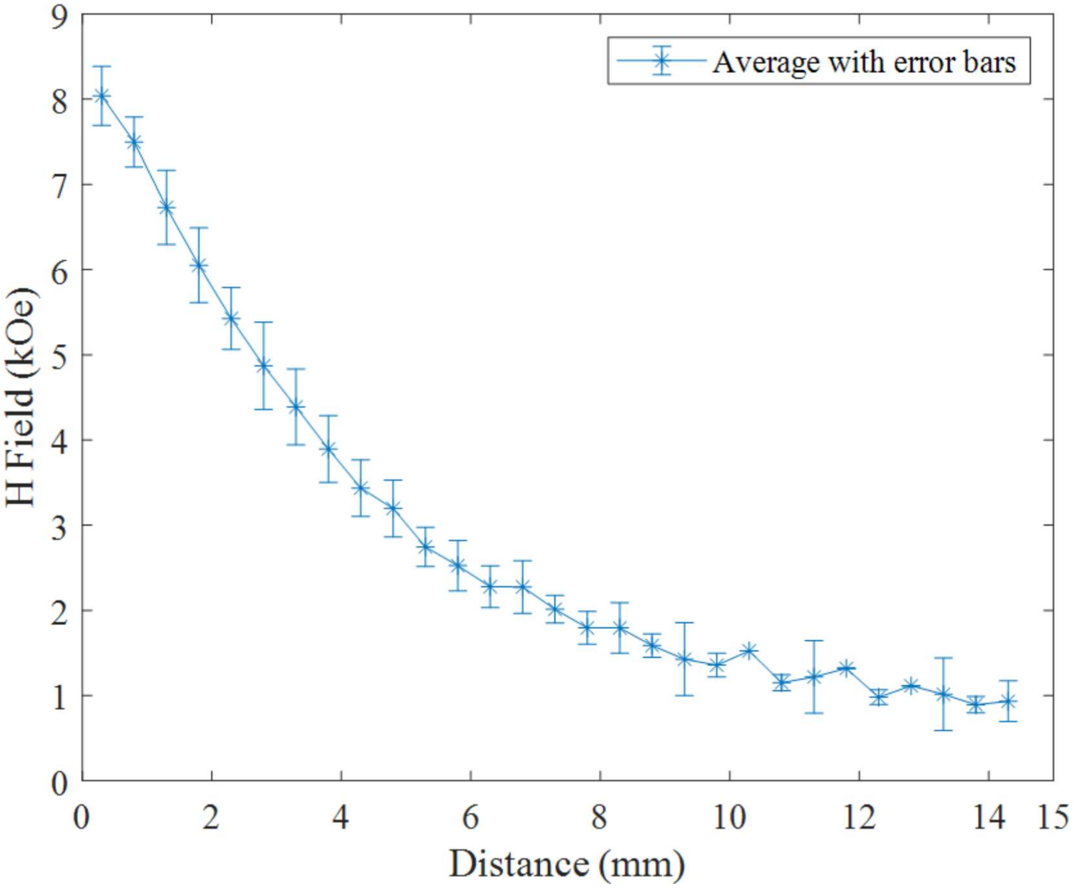

Figure 2.4 Field calibration curve. In this plot, the measured field and the separation distance between the top of the magnet stack and the sample location. This calibration curve averages 18 individual calibration curves. Error bars are included showing the accuracy of field calibration and its dependence with field.

After field calibration, the height on the z-stage was set to the value corresponding to the desired applied field. The AFM was initiated and necessary parameters for MFM were optimized to magnetic images with satisfactory contrast. It typically takes between 20 and 30 min to collect a complete set of AFM/MFM images at a given field value. Then, we varied the field by a predetermined step, corrected for any spatial drift, and collected a new set of AFM/MFM images. We repeated this operation until we reached the final field. Besides these in-situ field image collection, we also collected a series of images at remanence with varying magnetic history.

2.2 Computational Analysis: Binarization

We developed an image analysis software to count the number of domains and estimate the domain density, the principle metric of interest for this study. The software developed by previous members of the group was inefficient in analyzing large amounts of images and relied heavily on user input.

2.2.1 Principles and Overview

The binarization process reduces a fully colored image to a black and white image from which the number of domains is obtained without human counting. In MATLAB, binarization can be done via adaptive methods or global methods. The global method uses pixel intensity as a parameter and binarizes based on either the mean or median pixel intensity. The adaptive method applies the same process but introduces several parameters. The adaptive method is meant to handle variations in illumination on an image and thus does a type of local binarization. It calculates the pixel statistic based on a neighborhood of pixels that has a predetermined size. In addition, foreground and background objects can be indicated by a binary foreground parameter and a sensitivity parameter can be provided to increase the likelihood that a pixel is classified as a foreground object. We found that the global method does not produce sufficiently accurate binarizations, thus we used the adaptive method with the sensitivity being determined by a minimization function.

After the binarization step, the image is cleaned by removing pixel groups not meeting a minimum group size – usually around 35 nm^2 which is about half the area of the smallest domains observed. Morphological cleaning is also applied to remove noise from inherent to scanning. Individual magnetic domains are identified as group of neighboring pixels of same color.. Fig. 2.5 illustrates the entire process beginning with the original image followed by the greyscale conversion, the binarization, and the cleaning.

2.2.2 Sensitivity Parameter

In our analysis, the sensitivity parameter is determined by the same method acting on two different loss functions. The method uses MATLAB's minimizing function *fmnbnd* which utilizes the steepest gradient descent to find minimum of a provided loss function with respect to the sensitivity parameter.

The ratio loss R is defined as:

$$R = \frac{|B-W|}{B+W} \tag{2.1}$$

where B, W refers to the number of black and white pixels respectively. R is bounded between 0 and 1. In the formula, the absolute difference between the black and white pixels is divided by total number of pixels. Minimizing this ratio is particularly useful for binarizing remanent images as the minimum corresponds to a zero net magnetization which is expected in the OOP component of these samples. One disadvantage of this function is that as the total number of pixels increases the loss function becomes flatter. Additionally it can only binarize remanent images. R is constrained by the total number of pixels, T, defined as follows:

$$T = B+W,$$

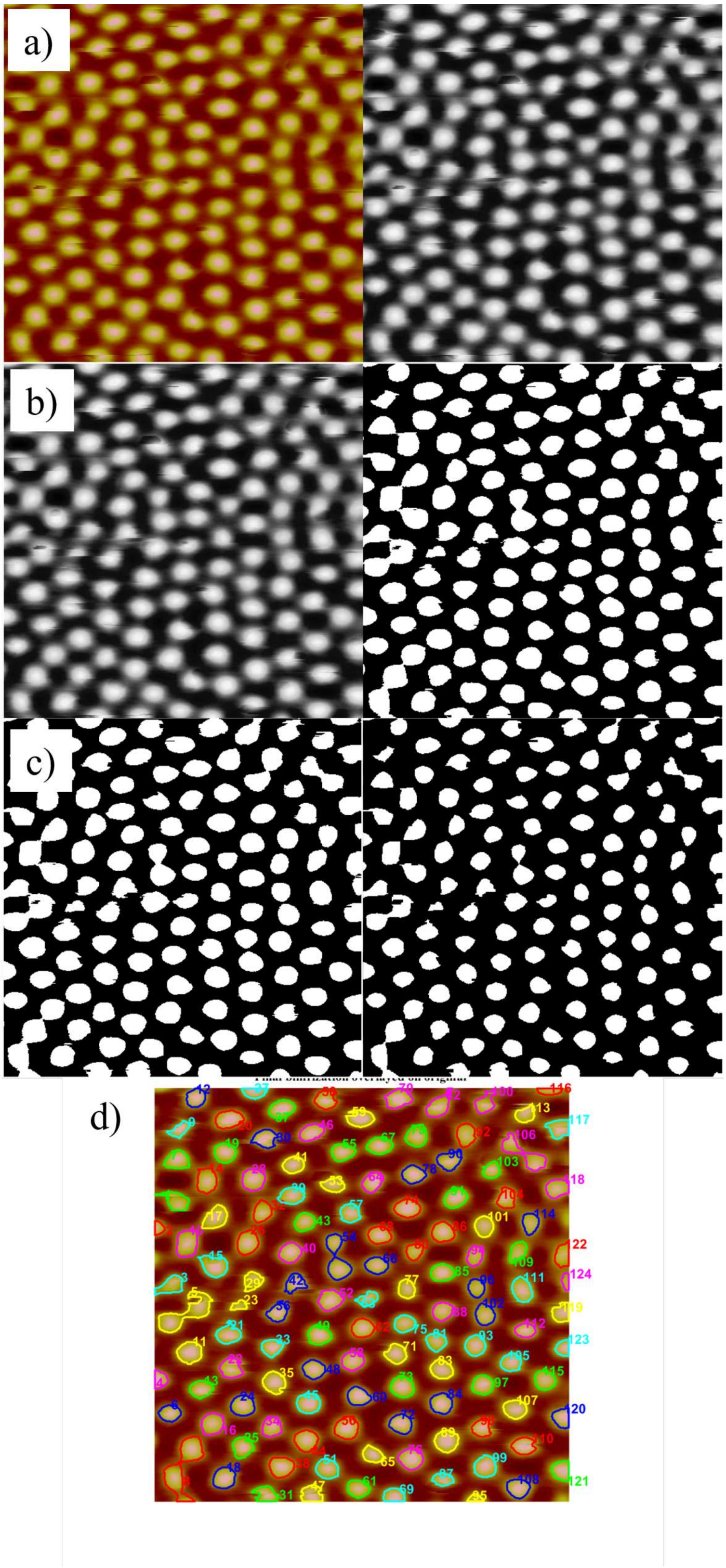

Figure 2.5 Illustration of the binarization process. The images follow the sequence: a) conversion from the original image to greyscale image, b) greyscale image to binary image via adaptive binarization, c) binary image cleaning via morpoilogical operations, and d) overlay of binary objects' perimeters onto original image.

thus we can rewrite the above as $R = |B - W|/T$. Thus for a given image whose T is constant, we find the following:

$$\begin{aligned}
\frac{\partial}{\partial s}T &= \frac{\partial}{\partial s}(B+W) \\
0 &= \frac{\partial}{\partial s}(B+W) \quad \text{(T is constant.)} \\
\frac{\partial}{\partial s}B &= -\frac{\partial}{\partial s}W
\end{aligned}$$

Thus taking the gradient of R we find

$$\begin{aligned}
\frac{\partial}{\partial s}R &= \frac{1}{T}\frac{\partial}{\partial s}|B-W| \\
&= \frac{1}{T} * \begin{cases} \frac{\partial}{\partial s}(B-W) & \text{if } B-W > 0 \\ \frac{\partial}{\partial s}(W-B) & \text{if } B-W < 0 \end{cases}
\end{aligned}$$

The minimization of R is scaled by T and may introduces size effects, unrelated to what we discuss later, into the binarization process: larger images have shallower slopes while small images have steeper slopes.

For non remanent images, when the net magnetization is non zero, one would need to modify the function by adding a constant biasing term to reflect the expected magnetization, which can be measured experimentally.

The absolute difference loss R_A is defined as:

$$R_A = \langle |GS - Bin| \rangle \tag{2.2}$$

where GS, Bin refers to the greyscale image and the binarized image. This function is bound between 0 and the max intensity (for greyscale images this is 256). This loss function is slightly more flexible than R and been thought to more suitable for the task of binarizing in general, but it has been demonstrated that R does better than R_A with remanent images. An explanation for this is that while R_A is indeed more flexible than R it loses local information by averaging, whereas R is more sensitive to local changes: a change in one pixel in R_A is much smaller than in R due to the fact that the greyscaled image pixel values range between 0 and 256 but binary images are only allowed to be $\{0,1\}$.

We use the ratio loss, R, for the remanent images and the absolute difference loss, R_A, for non-remanent images. Both methods do reasonably well for images with good resolution and limited noise. For images with poor resolution or lots of noise both methods lead to imperfect binarizations. That being said, most of our images have met the requirements for decent binarization.

2.3 Fast Fourier Transform Methods

In addition to binarizing images, we also looked at the Fourier transforms of the images as illustrated in Fig. 2.7. To do this we apply MatLab's *fft2d* onto the greyscaled images. We can also apply a change of coordinates from the cartesian coordiate system to the polar coordinate system as illustrated in Fig. 2.7.

Using these Fourier representations we integrated the signal to obtain the radial distribution as well as the angular distribution. We define the radial distribution function, RDF, and angular distribution function, ADF, as follows:

$$RDF(f(x,y)) = \int_0^{2\pi} |\mathscr{F}(f(x,y))| d\theta \tag{2.3}$$

$$ADF(f(x,y)) = \int_0^{R} |\mathscr{F}(f(x,y))| dr \tag{2.4}$$

, where f represents the original image and $\mathscr{F}$ is the Fourier transform. The upper limit R

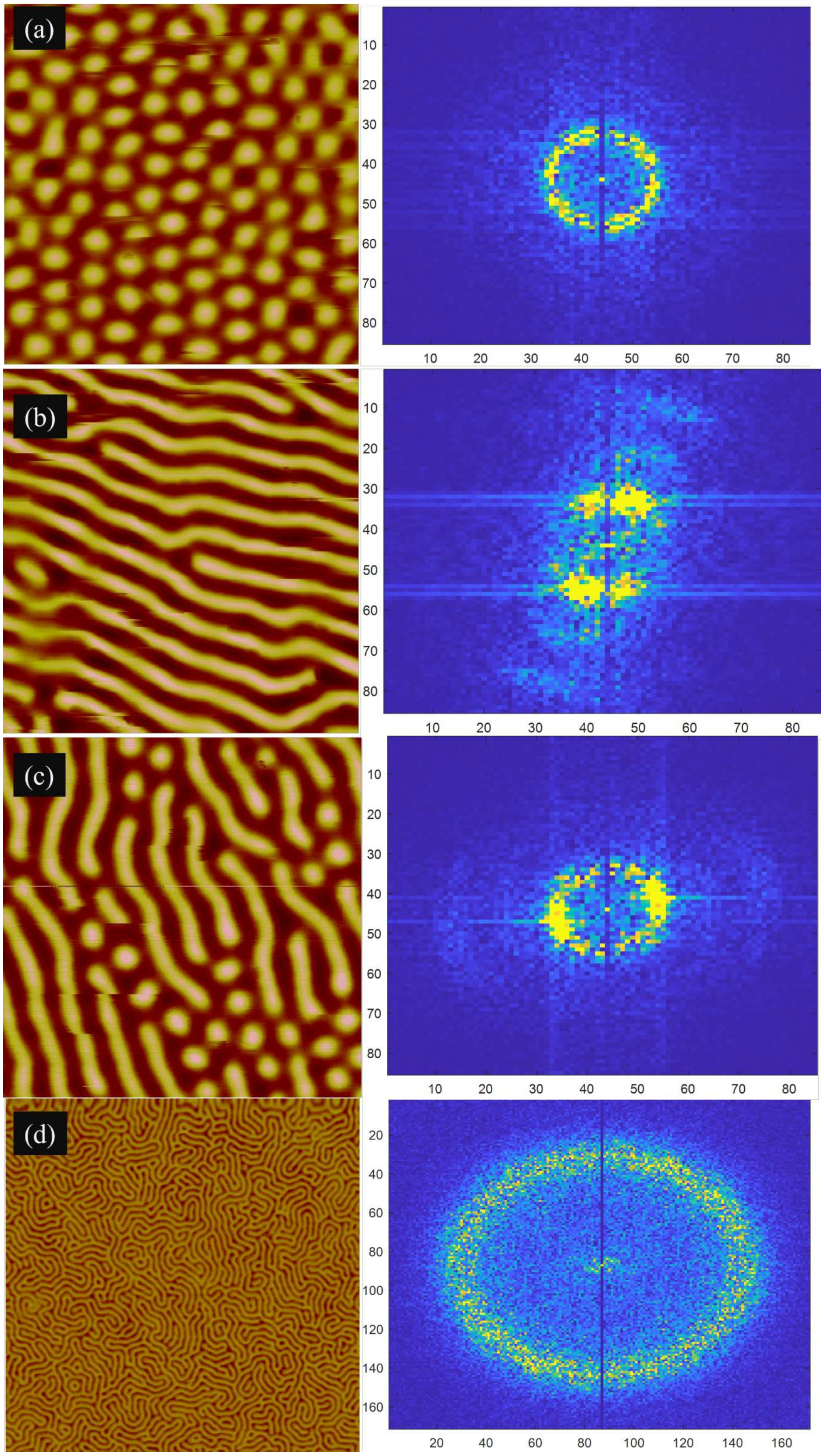

Figure 2.6 Fourier transforms for a selection of various magnetic domain patterns: (a) bubble pattern, (b) stripe pattern, (c) mixed pattern, and (d) maze state. The Fourier transform axes are in pixels.

corresponds to the maximum radius available in the Fourier transform. In Fig. 2.8 we see that a peak may exist in the RDF. When present, this peak reveals some magnetic periodicity in the pattern. The peak position R^* in the Fourier space is inversely proportional to the interdomain distance or magnetic periodicity.

Some exploration was undertaken to investigate alternative mathematical transforms to improve the accuracy of estimation of the magnetic periodicity. We have applied what we call a radial Fourier transform :

$$\mathscr{F}_{k_r,\theta} = \sum_{j=1}^{N_r} f_{r_j,\theta} e^{-2\pi i k_r r_j / N_r} \tag{2.5}$$

where r_j is the radial index in f, θ is a angle index in f, f is the image in the polar representation, k_r is the frequency domain variable, and N_r is the number of pixels along the radial direction. Similar to the peak observed in the RDF profile, we observe a peak in this radial profile, from which we extract the magnetic period.

2.4 Mapping of domain density and other characteristics

The binarization process was applied to more than hundreds of images and produced a large data set. Using the MATLAB's image processing toolbox we obtained the number of domains, size of domains and other metrics of interest. Domain density was obtained by dividing the number of domains by the imaging area. The domain density was scaled to 100 μm^2 area by multiplying by an appropriate scaling factor based on the actual image size.

We map the domain density with respect to the in-situ field H and the maximum applied field H_m and overlay an interpolated surface. We compared several methods of interpolation and found that a natural interpolator produces smooth surfaces. From these surfaces, contour maps were produced. This gives depth to the data and clarifies trends as demonstrated in the next chapter. We also produced maps for the magnetic period with respect to thickness and H_m.

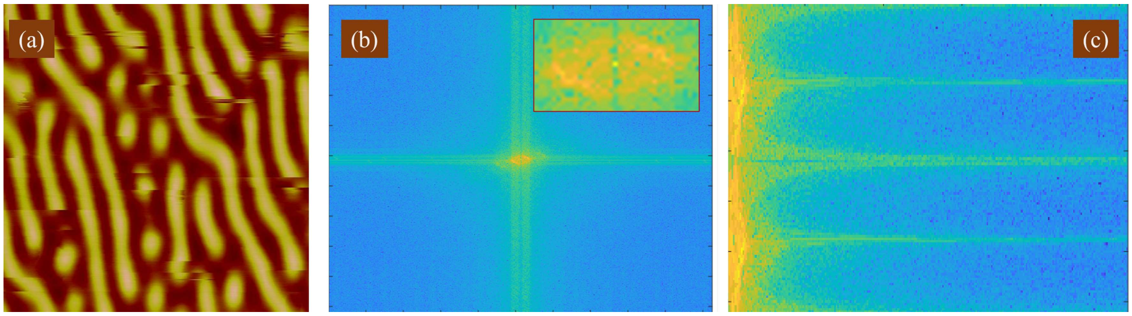

Figure 2.7 Example application of Fourier methods: (a) Initial MFM image. (b) Fast Fourier transform of image (a). (c) Fourier transform of image (a) represented in polar coordinates

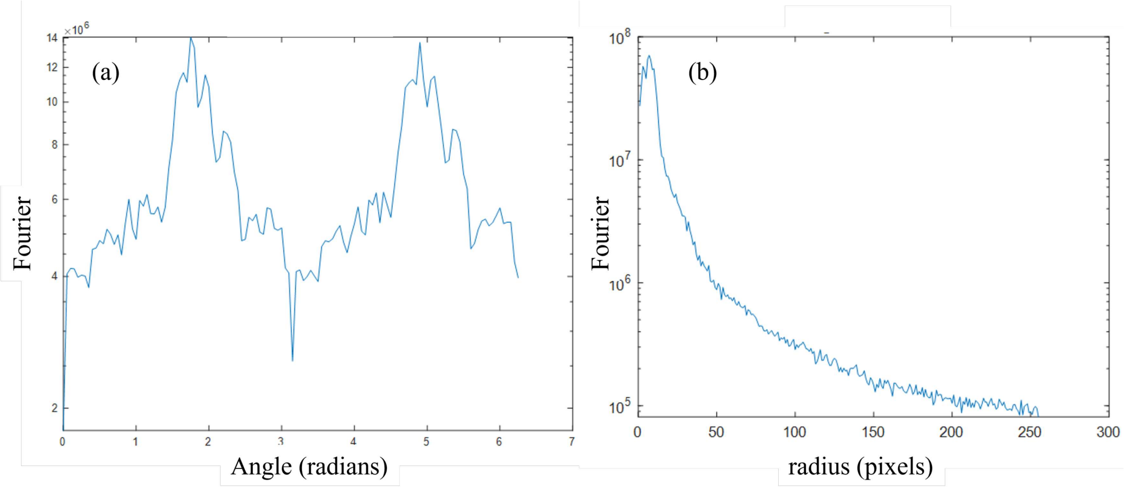

Figure 2.8 (a) The angular distribution of the MFM image shown in Fig. 2.7. (b) The radial distribution (RDF) of the the MFM image shown in Fig. 2.7.

Experimental errors that arose during calibration were corrected. One systematic error that occurred was the discrepancy between field measured by the probe and the field actually experienced by the sample due to the difference in their respective thickness. We used either the average calibration graph mentioned in section 2.1.2 or interpolated between points to find the correct field values. Another error that occurred was error due to the size of the image scan. We will discuss this error in the results chapter. Random error was corrected by removing outliers in image data sets using a moving average of three points and a criterion of three interquartile ranges as the cutoff. The surfaces and data are presented with the corrected data.

Chapter 3

Results

3.1 Image Finite Size Effects

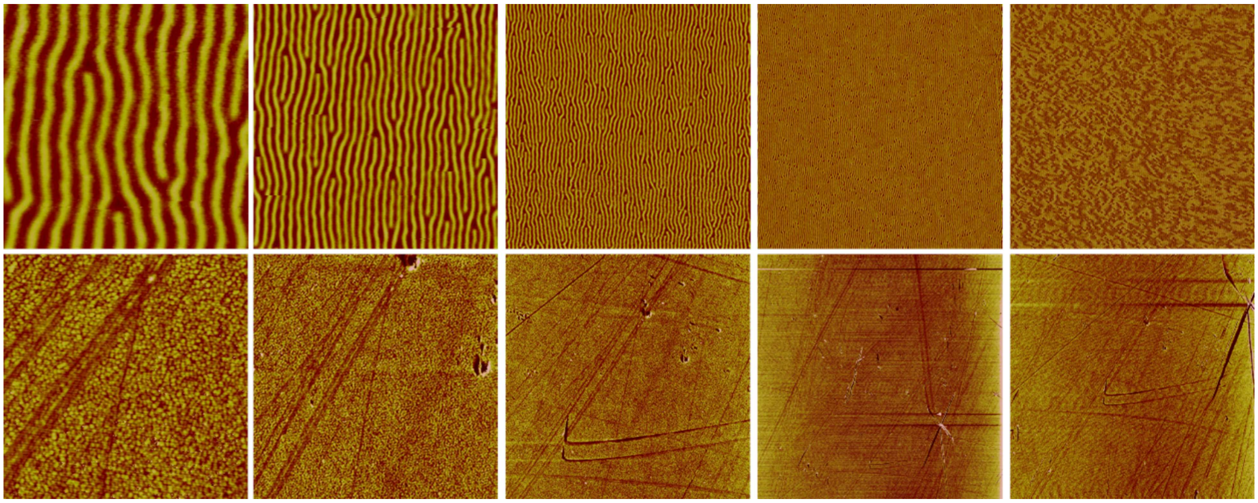

Figure 3.1 Left to right shows MFM images (top) and corresponding AFM images (bottom) with increasing image sizes of $2 \times 2,\ 4 \times 4,\ 10 \times 10,\ 25 \times 25,\ 40 \times 40\ \mu m^2$ at $H_m = 4$ kOe for sample A145 N = 20.

Above we have Fig. 3.1, which demonstrates the effects of finite size images for the sample A145 N = 20. For the in-situ studies that follow, image sizes were limited to less than $4 \times 4\ \mu\text{m}^2$ for effective time management. As a result, smaller images led to domains being cut of leading to incorrect domain densities.

To investigate the behavior of image size effects we look specifically at the domain density as a function of image size. In Fig. 3.2, we plot the domain density for the domains with aligned and reversed magnetization with respect to the applied field, for the sample A145 N = 20 at $H_m = 4.0$ kOe. The domain density for both the aligned and reversed domains decays rapidly with image size and before reaching a plateau between 10 and 20 μm. This shows that when the image size is below 10 μm the domain density is drastically affected by the image size is artificially increased by several factors when the image size is reduced from 10 μm to 2 μm. This behavior indicates that the variation due to finite size effects becomes significant below a certain size. The image size at which the domain density starts to plateau depends on the type of domain pattern.

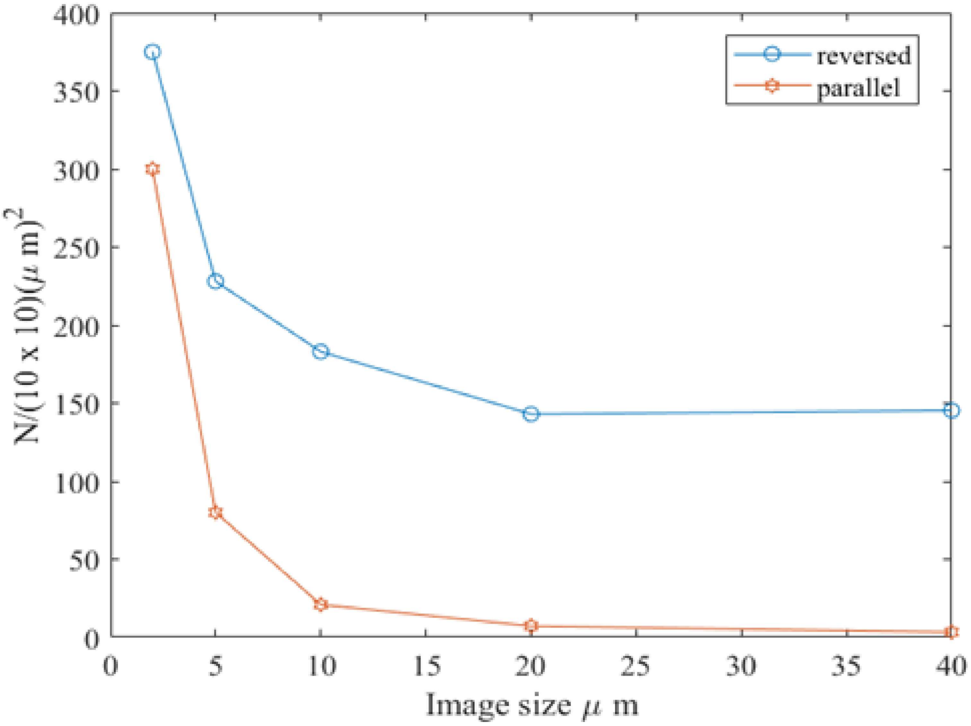

Figure 3.2 Domain density as a function of image size for A145 N=20 at $H_m = 4$ kOe

We split the 40×40 μm^2 image into 400 2×2 μm^2 images and investigate variation in domain

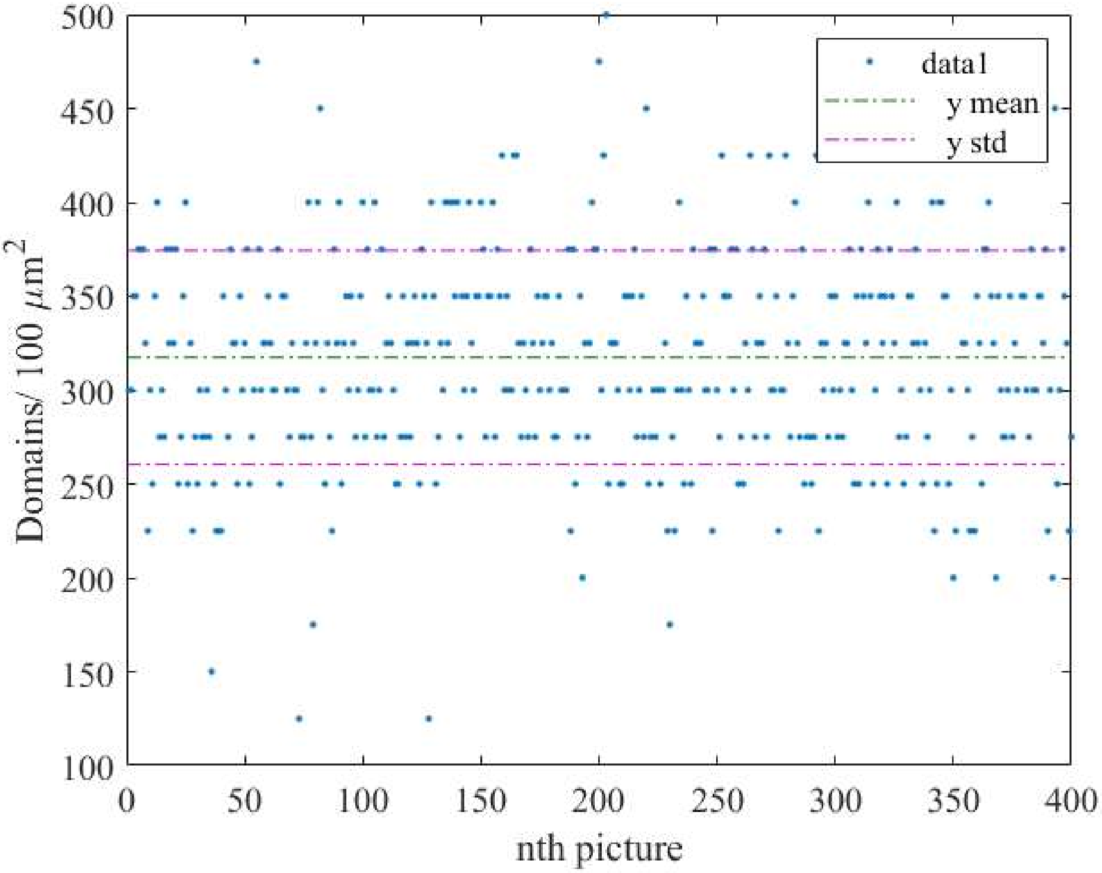

Figure 3.3 Variation in the domain density through individual images for partition size of 2×2 μm^2

density while going through individual partitioned images as shown in Fig. 3.3. The standard deviation for this sample is approximately ±50 domains per 100 μm^2 with an average of 315 domains per 100 μm^2. From this analysis, we have a decent approximation of the uncertainty when estimating the density on a single 2×2 μm^2 image that is about 50/315 = 15%. Increasing the number of images does not improve the domain density accuracy towards that of 40×40 μm^2 image. This shows that finite image size effects are not statistical but related to real truncating effects at the edge of the image.

We expanded this study to include various patterns in a paper that has been accepted for publication [10] in the AIP Advances journal (see manuscript in the Appendix A A). In this study we investigated three distinct patterns: stripe, bubble, and a mixed pattern. From our analysis we established finite size effects for these three different types of patterns, as summarized in Fig. 3.4.

We found that for bubble patterns at small images sizes ($< 2\ \mu m$) domain density is not too much affected by the image size, with an excess density of only 1% when reducing the size to 2 μm. . For the mixed pattern we observed about an excess density of about 50% when reducing the image size to 2 um, and for the stripe we observed an excess density up to 400% at similar image sizes. This large differences in excess density depending on the pattern type can be explained by the fact that stripes have much longer domains than bubble domains. Consequently, smaller image sizes arbitrarily cut of the domains and artificially increase the domain density.

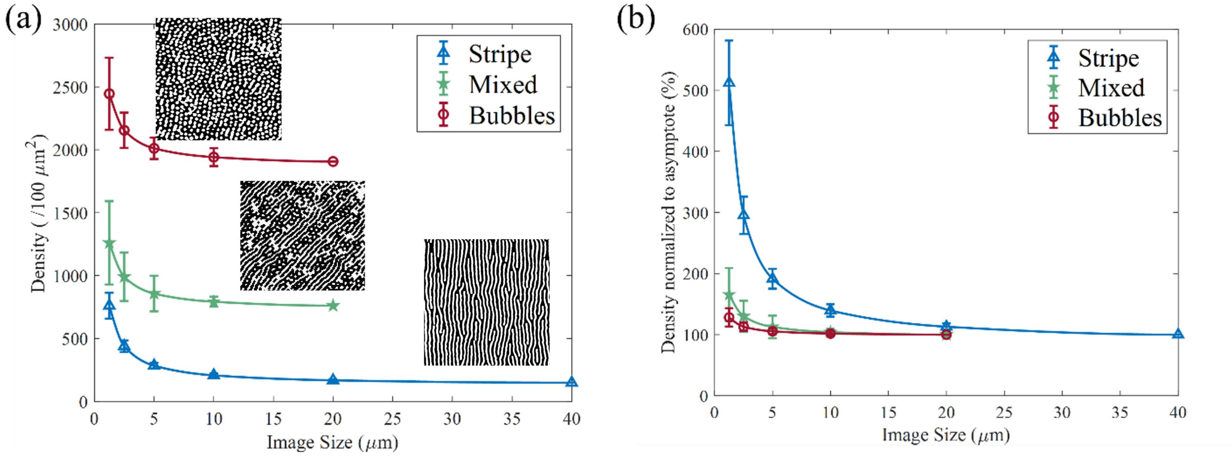

Figure 3.4 Comparative denisty plots for the stripe, mixed and bubble states. (a) Density of reversed domains as function of the image size it is estimated on, with interpolated curves; (d) Same density curves, normalized to their asymptotic value for comparison purposes.

We calculated the excess density at several images sizes as well as its gradient with respect to image size and complied them into table 3.1.

We found that finite size effects evolve both as a function of pattern (from bubble to stripe) and

	Excess density $\Delta\rho(\%)$ at various L				Cutoff (minimum) image size (μm)	
Morphology	10 μm	5 μm	2.5 μm	1.25 μm	$\Delta\rho < 10\%$	$\Delta\rho < 1\%$
Bubbles	1.8%	5.5%	13%	28%	3.2	12.9
Mixed	4.1%	13%	30%	66%	6.2	15.6
Stripes	39%	91%	195%	412%	23	35

Table 3.1 Selected values for the excess density and cutoff image sizes for the various morphologies: bubble, mixed and stripe states, where the bubble diameter and stripe width are both around 100 nm. The excess density ρ, here listed for various image sizes L, is normalized to the asymptotic density value and provided in %, (also see Fig. 3.4). The cutoff image size is estimated using various criteria: the normalized excess density $\Delta\rho < 10\%$ and 1%.

image size. For stripe or maze patterns,the excess density increases more rapidly when decreasing image size and as the pattern moves toward longer domains. Based on the above results it is recommended that for bubble patterns a minimum image size of approximately 13×13 μm^2 should be used for accurate statistics (limiting the excess density to 1%), similarly 35×4 μm^2 images should be used for stripe patterns.

3.2 Remanent Domain Density for A145 (30 Å, N=20)

We collected a series of remanent images on sample A145, where the magnitude of the previously applied field H_m was varied from (max value) down to (min value). We extracted the domain density in the remanent images and plotted it as a function of H_m. In Fig. 3.5,our measured domain density is plotted against previous data published in [5] and [7], which shows an excellent agreement. H^* indicates the magnetic field where the optimal domain density is found around $H^* = 8.7$ kOe, at which point the domain pattern has evolved into a bubble pattern.

This observed morphological behavior observed at remanence has now been consistently observed in several Co/Pt multilayers with different several bi-layer repeats and thicknesses.However, the morphological changes in the domain pattern while applying a field in-situ has not been yet

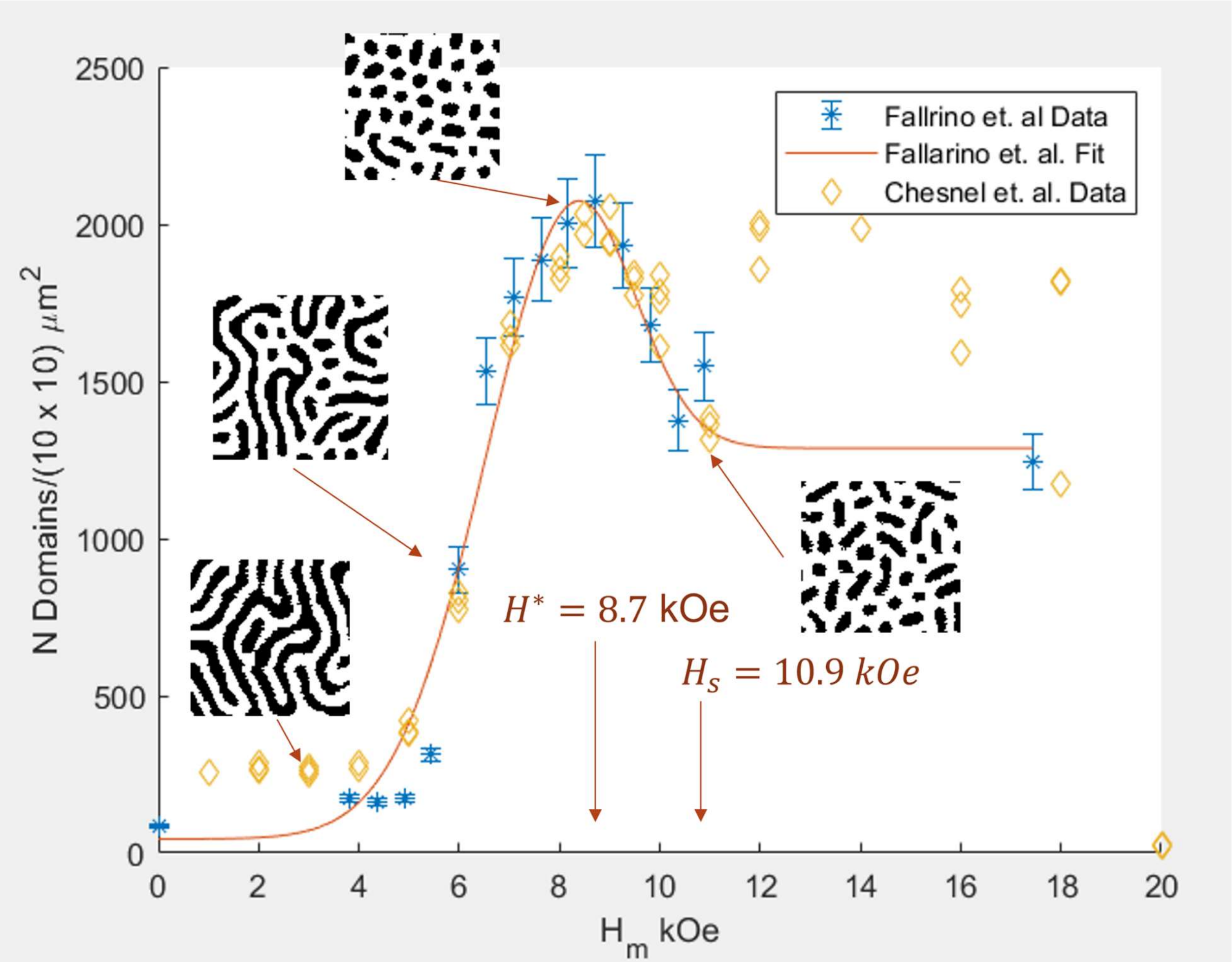

Figure 3.5 Domain density at remanence as a function of previously applied field H_m. Our data is compared to previous data published in Fallarino et. al. paper [7] and data taken in the Chesnel lab for sample A145 -[[Co(31Å),Pt(7Å)]$_{20}$. H^* is the field at which the peak domain density occurs and H_s is the saturation field of the sample. The insets are snippets from the binarized images collected at field values indicated on the diagram by arrows.

investigated in the literature to the best of our knowledge. We next investigate how the domain density evolves with applied magnetic field, $H_{\text{in-situ}}$.

3.3 Domain Density of Minor Descending Branch for A145 (30 Å, N=20)

The sample A145 is composed of [Co(t),Pt(7Å)]$_2$0 with cobalt thickness of t = 30 Å and N = 20 bilayer repeats. For this sample, saturation occurs at $H_s = 11$ kOe whereas the remanent peak domain density occurs at an optimal field $H_m^* = 9$ kOe, that is about 80% of the saturation field [7].

We surveyed this sample by taking a series of in-situ images using the setup described earlier. We began this study at $H_m = 7$ kOe and descended to the minimum field of 3 kOe. In some series, we were able to image the remanent pattern at locations near where the in-situ series was collected. The largest H_m we were able to apply in-situ was 7.0 kOe which is somewhat lower than the field values for the remanent study and H_s = 11 kOe.

Qualitative analysis, see Fig. 3.6 and Fig. 3.7, reveals that the morphological transitions observed in the remanent studies support our observations in the in-situ studies. Furthermore, we can distinguish three types of in-situ behaviors occurring for ranges of H_m values. The first morphological phase (Phase I or Stripe Phase) occurs when $H_m < 3.8$ kOe: the domain patterns remain in a stripe state. The second morphological phase (Phase II or Transition Phase) occurs when $3.8 < H_m < 5.4$ kOe: the domain pattern evolves from a bubble state at H_m down to a short stripe state at $H_m = 0$ kOe. The third morphological phase (Phase III or Bubble Phase) occurs for $H_m > 5.4$ kOe: the domain pattern remains in a bubble state when H is decreased from H_m to 0 kOe.

To identify these different phases quantitatively we binarized the images and used counting methods described earlier. In Fig. 3.8, we see that the domain density increases drastically as a response to both H_m and $H_{\text{in-situ}}$. In the plotted range, the response to H_m appears more drastic than the response to $H_{\text{in-situ}}$.

In the remanent study the domain density peaked at the $H^* = 9$ kOe but the mapping above is limited to H < 7 kOe region. We can therefore predict that the density would continue to increase if

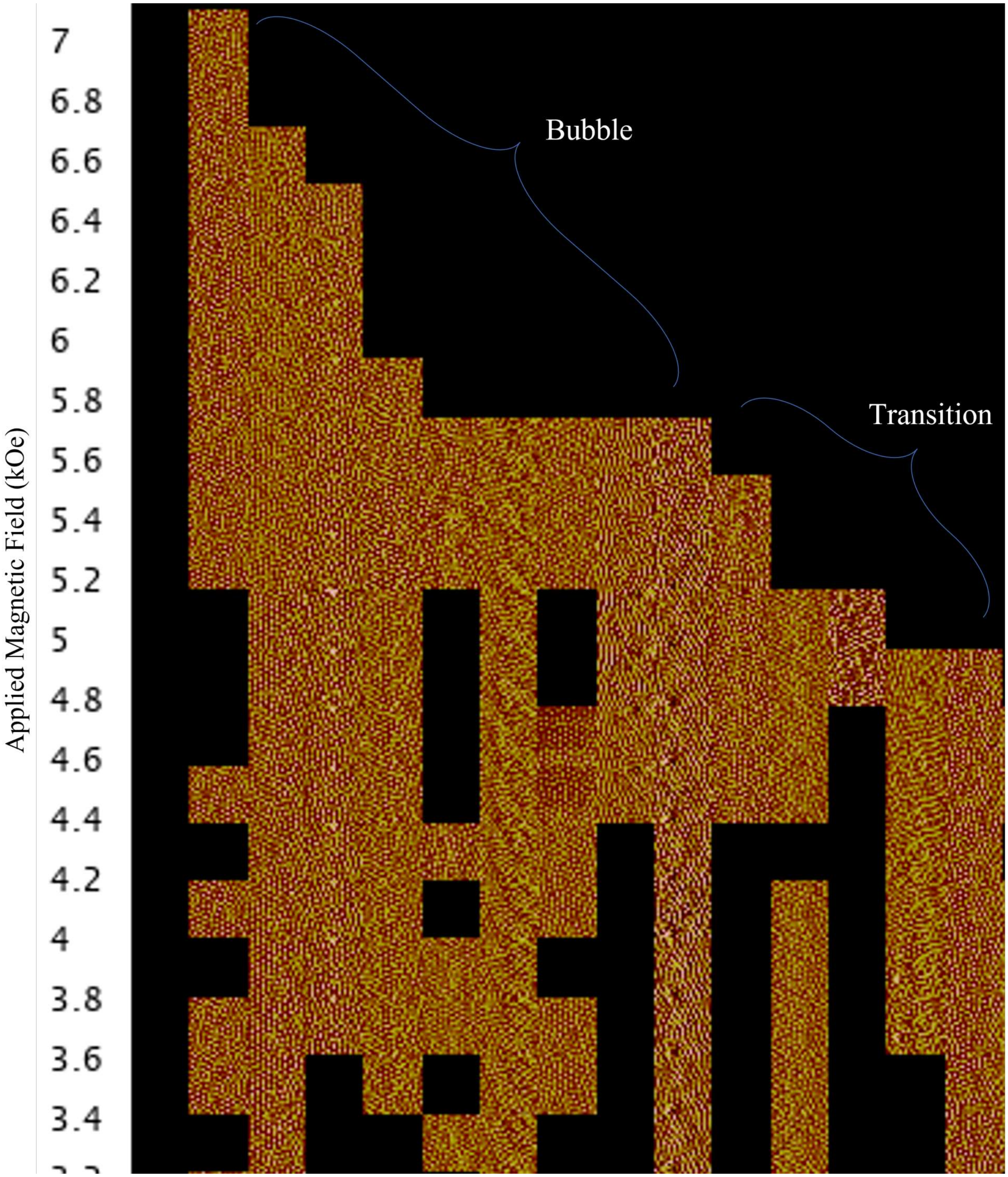

Figure 3.6 First qualitative map of the morphological stable phase and transitions regions for $[\mathrm{Co}(31\text{Å}),\mathrm{Pt}(7\text{Å})]_{20}$ in the region $7.0\ \mathrm{kOe} \leq H_m \leq 5.0\ \mathrm{kOe}$. The in-situ field value is indicated to the left and phases are labeled.

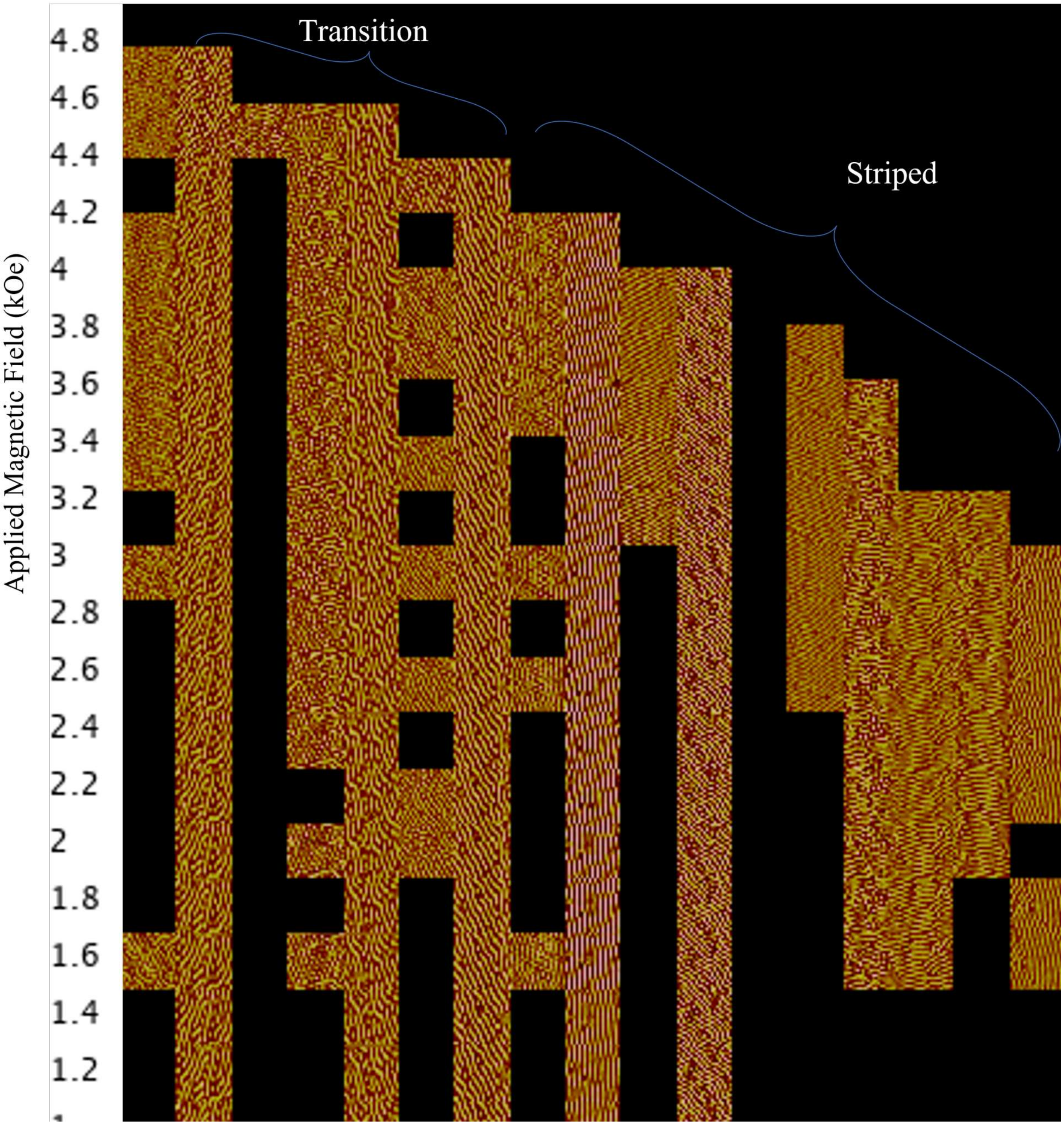

Figure 3.7 Second qualitative map of the morphological stable phase and transitions regions for [Co(31Å),Pt(7Å)]$_{20}$ in the region 4.8 kOe $\leq H_m \leq$ 3.0 kOe. The in-situ field value is indicated to the left and phases are labeled

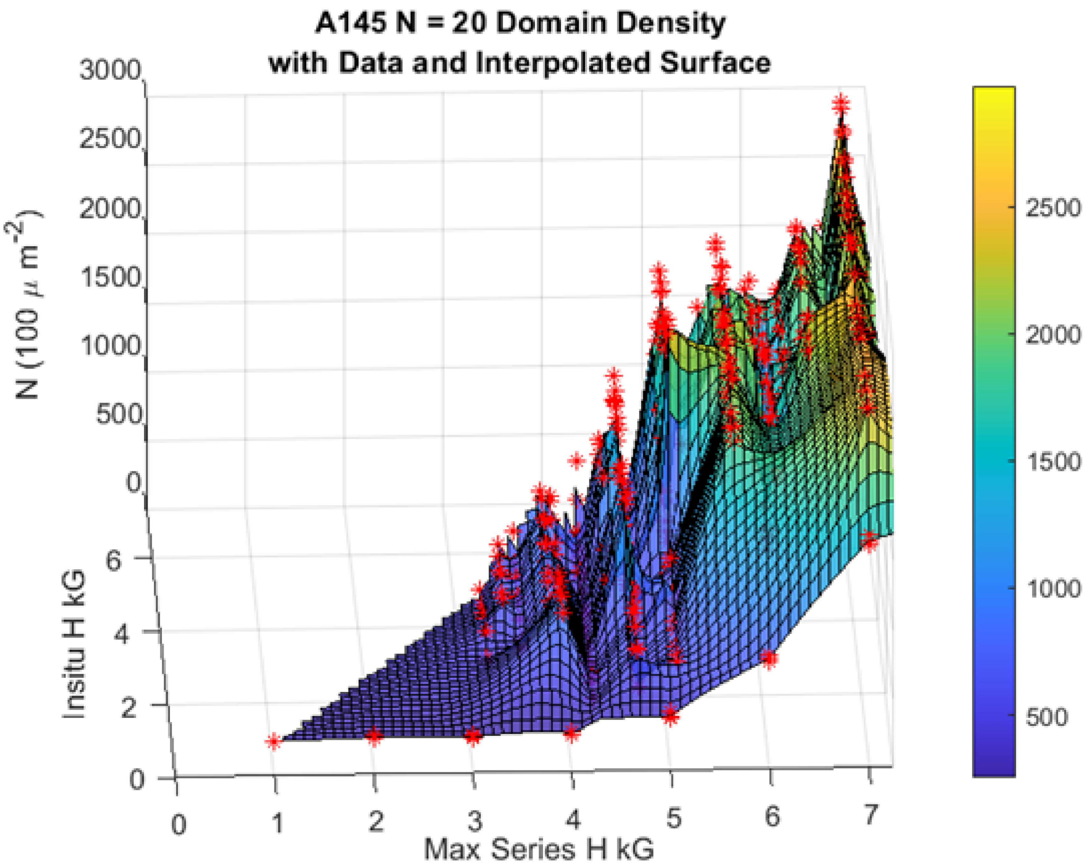

Figure 3.8 Domain density surface as response to maximum applied field H_m and applied field $H_{\text{in-situ}}$ for [Co(31Å),Pt(7Å)]$_{20}$

.

we could increase the in-situ field. Despite being in the sub-H^* region, one series, $H_m = 7.2$ kOe, reaches a maximum domain density 2700 domains/100 μm^2 with a resulting remanent value of 1800 domains/ 100 μm^2. This quite large difference shows a non-trivial increase in domain density due to applied field. From our qualitative analysis, we estimate that bubble domains occur above 5.0 kOe, which agrees with our subsequent density map. Based on these observations, we can say that the cutoff of 2000 domains/100 μm^2 is indicative of transitioning into a bubble state. We map the phase transitions onto the domain density map.

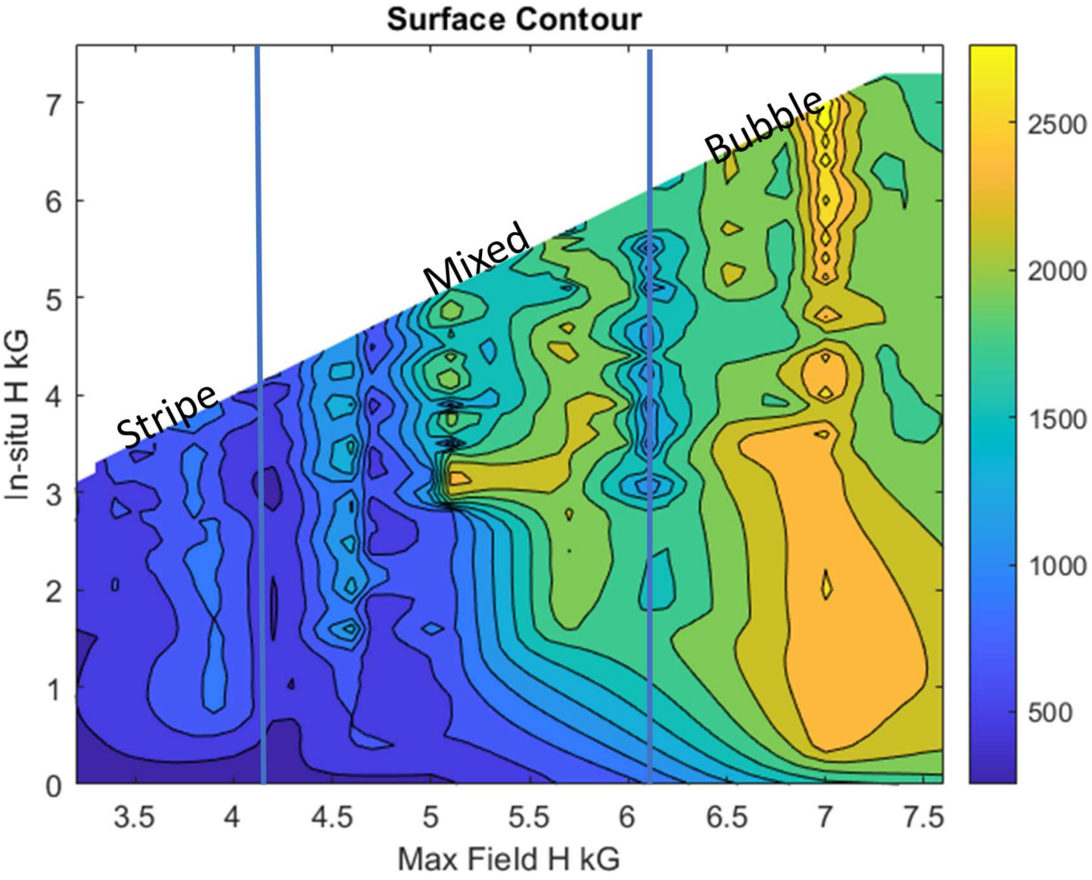

Figure 3.9 Domain density contour with morphological states labeled for[Co(31 Å),Pt(7 Å)]$_{20}$. The color-bar indicates domain density in domains/ 100 μm^2.

3.4 Domain Density of Full Hysteresis Loop for A827 (10 Å, N=20)

The sample A827 is composed of [Co(10 Å), Pt(7 Å)]$_{20}$ This sample is interesting because it has a low saturation point of approximately $H_s = 4.0$ kOe effectively allowing us to investigate a full hysteresis loop with in-situ magnetic field – unlike the previous sample A145 whose saturation point is 11 kOe.

For A827, we find that the domain density peaks at $H^* = 3.2$ kOe. As the field is increased, the

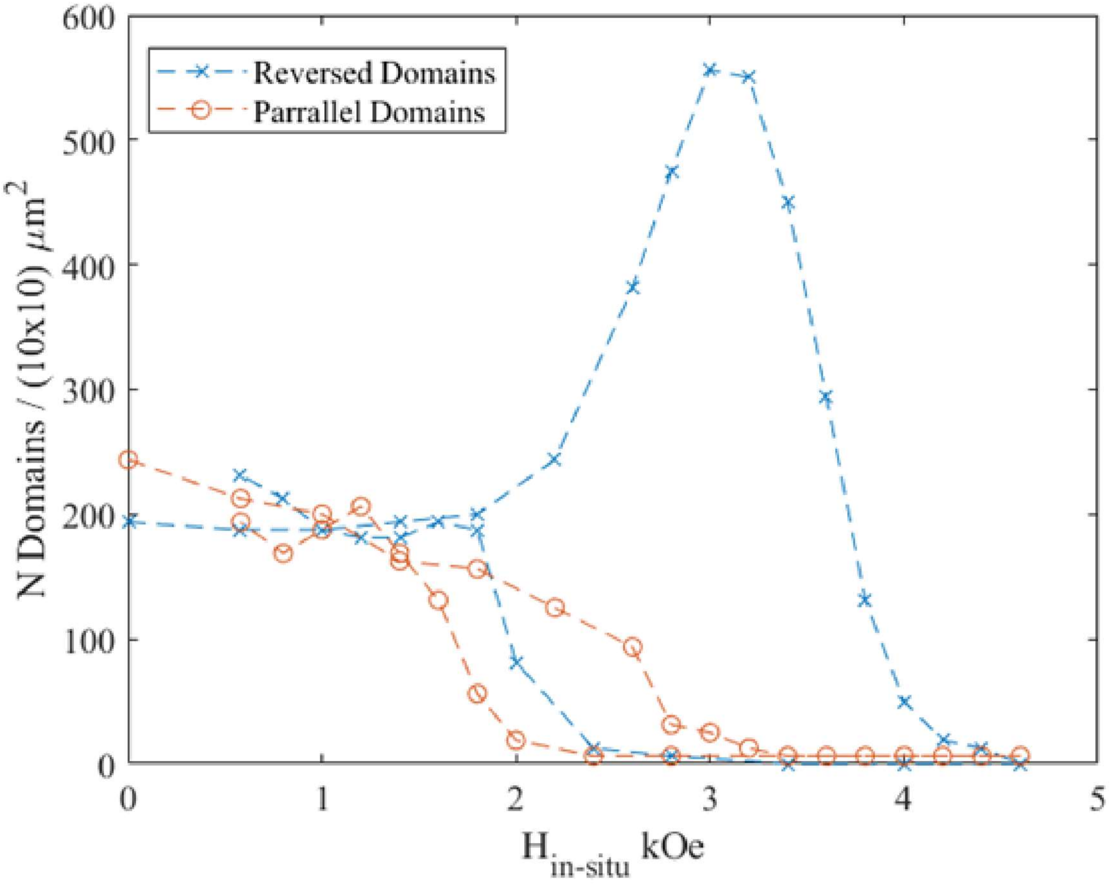

Figure 3.10 Full hysteresis branch domain density for [Co(10Å),Pt(7Å)]$_{20}$ at $H_m = 4.4$ kOe.

domain density decays to 0 as the sample reaches the saturation field, $H_s = 4.4$ kOe. We note that the peak domain density occurs at $H^*/H_s = 0.72$ which is in the same range as A145 $H^*/H_s = 0.8$. When coming back from positive saturation – decreasing the in-situ field back to zero – the domain density approximately retrieves its original value of 200 domains/ 100 μm^2 . The peak density is approximately 550 domains / 100 μm^2 which is almost three times the remanence density (200 domains/ 100 μm^2). A qualitative analysis of the images reveals that the domain pattern does not go into a pure bubble state except near saturation which explains why the domain density does not reach the domain density of typical remanent bubble states.

We have also begun a preliminary study across the whole space of field values as seen in Fig. 3.11 which shows domain density mapped as a function of H and H_m, for the ascending branch and the descending branch respectively. On the ascending map, a clear peak appear at around $H^* = 3$ kOe, consistent with the single loop result in Fig. 3.10.

3.5 Magnetic Periodicity at Remanence

We focus here on the $N = 20$ series at remanence to investigate the magnetic periodicity at thicknesses of $10, 15, 20, 25,$ and 30 which correspond to the samples A827, A826, A825, A824, and A145 respectively. In each sample, the data suggest peaks occurring with respect to H_m as seen in Fig. 3.12.

We see peaks in the magnetic period occurring near $H_m = 9, 7, 7, 5, 3.5$ kOe for samples A145, A824, A825, A826, and A827 respectively. This suggests a correlation between Co thickness and the H_m of peak magnetic period, $H_m^{p^*}$. These findings are consistent with the observed peaks in the domain density in the case of A145. This result may seem counter-intuitive at first as increasing domain density would imply compactification of domains and thus smaller magnetic periodicities. It is possible, however, to justify this behavior on morphological grounds. Suppose that we have an ideal stripe morphology with an interdomain distance of p. If the morphology were to transform via fragmentation into a hexagonal lattice the inter-domain distance would necessarily have to increase as the domains shift into hexagons the interdomain distance (or magnetic period) becomes $p \to \sqrt{2}p$.

Finally, we mapped, in Fig. 3.13, mean magnetic period, as a function of Co thickness and H_m. This preliminary map suggests that there exist some correlations between the Co thickness, the applied field H, and the observed magnetic periodicity. This remains to be further investigated.

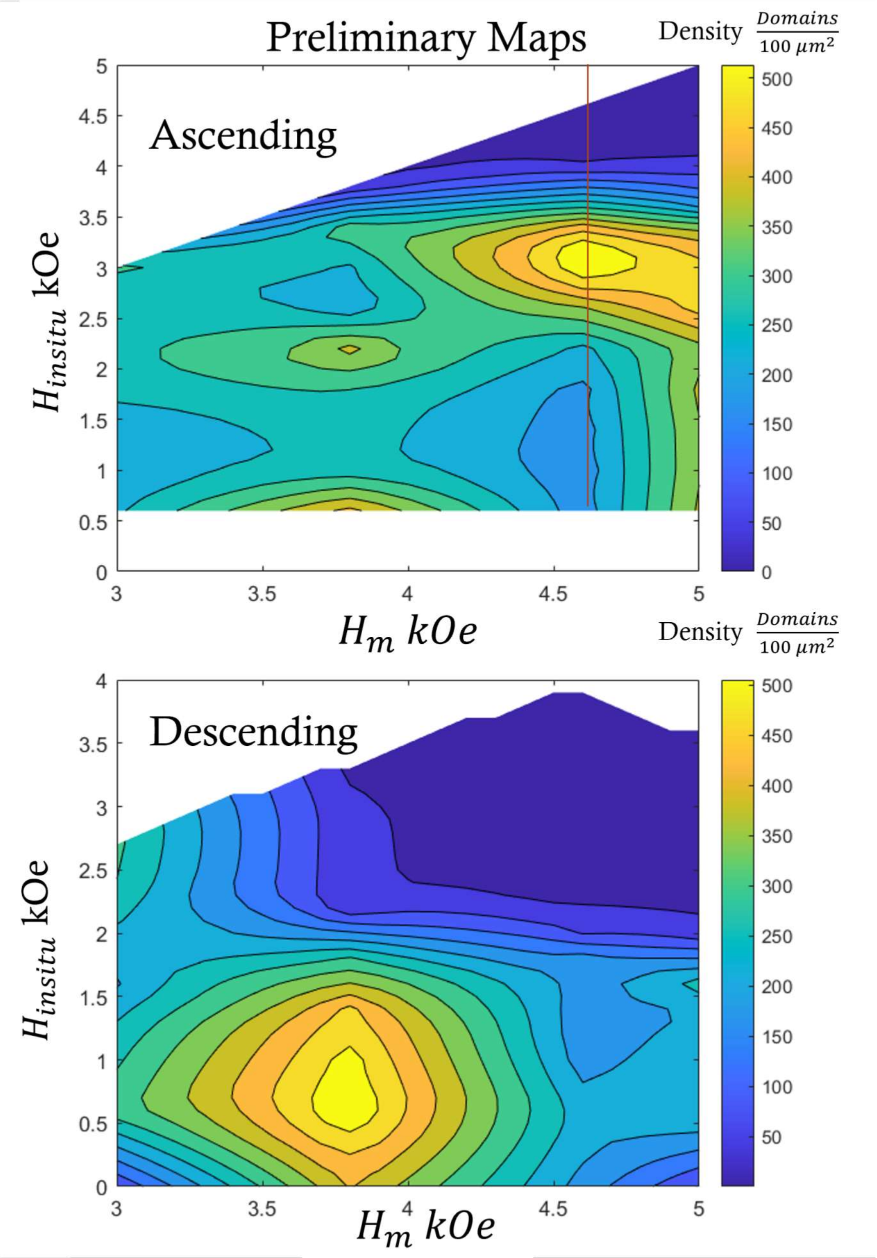

Figure 3.11 Domain density surface as response to previously maximum applied field H_m and applied field $H_{\text{in-situ}}$ for $[\text{Co}(10\ \text{Å}), \text{Pt}(7\ \text{Å})]_{20}$. Orange line in ascending map indicates location of full hysteresis loop.

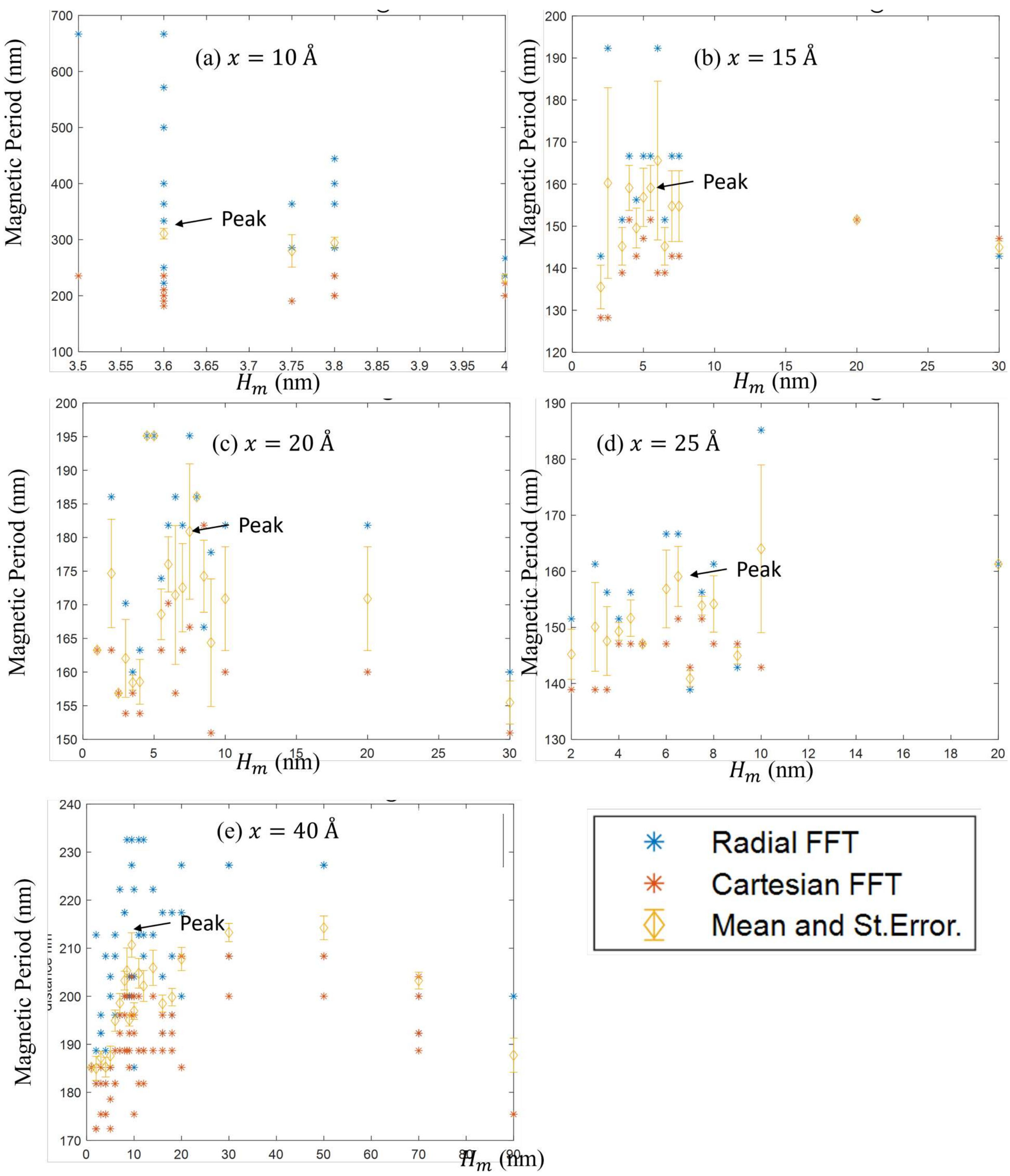

Figure 3.12 Magnetic periodicity curves plotted with respect to the maximum previously applied field H_m. The Cartesian method refers to traditional Fourier transforms while the radial method refers to radial Fourier transforms described in Ch. 2.3. x is referring to the Co thickness in each sample. (a)-(e) are samples A827 - A824, and A145 respectively.

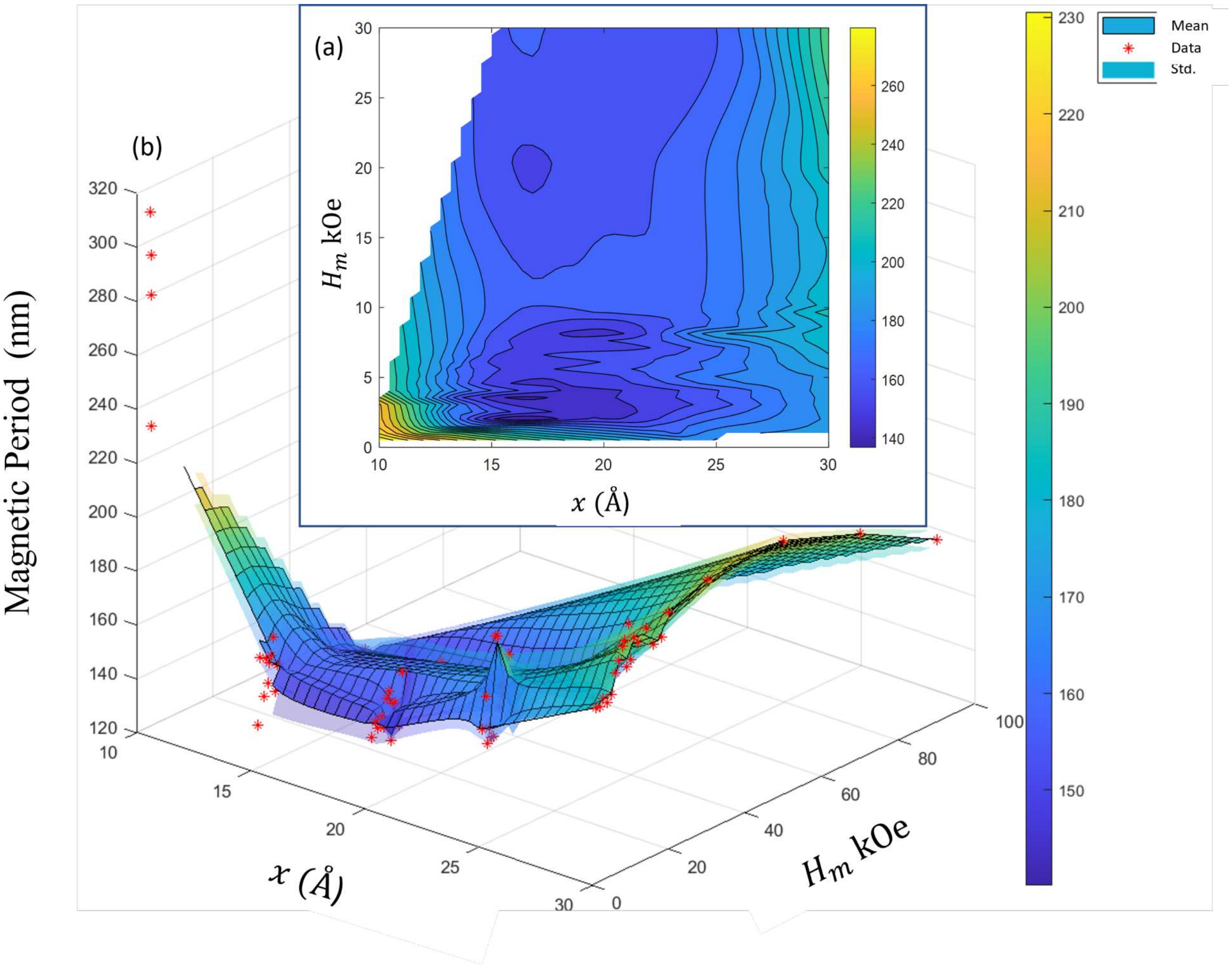

Figure 3.13 Magnetic periodicity, mapped as a function of Co thickness x and previously applied field H_m. Inset (a) represents a top view of (b) as a contour map. Error is the standard deviation from the mean while natural indicates the interpolation between data points.

3.6 Conclusion

We have investigated finite images size effects and their role in biasing the domain density. We found that the estimation of domain density may be significantly altered by finite size effects, particularly in the case of stripe patterns and optimization for magnetic nanotechnologies.

We have completed in-situ surveys of the magnetic domain patterns and associated morphological transition under various conditions in various samples. This included in-situ data for A145 ([Co(31 Å), Pt(7 Å)]$_{20}$) for applied magnetic field, 7.0 kOe $\leq H_{\text{in-situ}} \leq$ 0 kOe with 7.0 kOe $\leq H_m \leq$ 3.0 kOe. We have mapped the domain density as a function of H and H_m and compared our results with results obtained at remanence for that same sample. We discover three distinct morphological phase transitions occurring with response to in-situ applied magnetic field: bubble, transition, and stripe. These transitions are novel and indicate the evolution of domains in response to applied field. However, the region over which we have surveyed limited to a field region below the optimal field value H* that maximizes the remanent domain density.

On the other hand, we have begun in-situ surveys of sample A827 ([Co(10 Å),Pt(7 Å)]$_{20}$) , through the saturation region, 5.0 kOe $\leq H_{\text{in-situ}} \leq$ 0 kOe with 5.0 kOe $\leq H_m \leq$ 3.0 kOe thus effectively capturing the behavior of full hysteresis loops. We have begun preliminary analysis and see a significant increase in the domain density as a response to applied field compared to remanent conditions. This provides interesting dataset complementary to the dataset on A145.

Additionally, for the series $N = 20$, we have investigated the magnetic periodicity as a function of Co thickness and H_m. We found that there are indication of some correlation between the magnetic period and the Co thickness as well as the previously applied field H_m , that supports our findings on the domain density.

Further studies should be conducted varying bi-layer repeats, N, for [Co(31 Å), Pt(7 Å)]$_{\text{N}}$ to understand the in-situ response in conjunction with N. Insights of these studies will be beneficial in understanding the physics of multilayers.

Appendix A

Publication about Finite Size Effects

The following publication, as described earlier in chapter 3, is to be published in *AIP Advances* which gives the copyright to the authors under the creative commons license. My role in this paper was as the producer of the data analysis and associated figures. I also helped to write the methods section and to revise the document.

Finite image size effects on the characterization of magnetic domain patterns via magnetic force microscopy

Michael Vaka[1], Joey Ray[1], Misael Campos[2], Karine Chesnel[1,a)]

[1]Department of Physics and Astronomy, BYU, Provo, UT, 84058, USA

[2]Department of Electrical Engineering, Princeton University, Princeton, NJ, 08544, USA

a) Author to whom correspondence should be addressed: kchesnel@byu.edu

Abstract

Optimizing magnetic thin films for nanotechnologies often requires imaging nanoscale magnetic domain patterns via magnetic microscopy. The finite size of the image may however significantly affect the characterization of the observed magnetic states. We evaluated finite image size effects on the characterization of a variety of stripe and bubble domain patterns exhibited by ferromagnetic Co/Pt multilayers with perpendicular magnetic anisotropy, where the domain size (stripe width and bubble diameter) is around 100 nm. If the image size is too small, below ~ 5 μm, it may cause a significant underestimation of average domain size and overestimation of domain density by up to a factor 5 when reducing the image size from about 20 μm to about a 1 μm. Using a criterion based on how the excess density evolves with image size, we found that to obtain reliable statistical estimates of domain density and average domain size, the image needs to be large enough, and include at least about 100 stripes or about 2500 bubbles.

Introduction

Magnetic recording nanotechnologies heavily relies on the optimization of magnetic media. In the quest for ever-increasing storage capabilities, thin ferromagnetic films exhibiting perpendicular magnetic anisotropy (PMA) have been key materials as they allow achieving high density of nanoscale magnetic domains. [1-5] Thin Co/Pt and Co/Pd multilayers with PMA are such materials that exhibit high magnetic domain densities [6-8], and where the domain pattern can serve as a template for magnetic domain memory applications [9,10]. We found in previous studies on $[\mathrm{Co}(x)/\ \mathrm{Pt}\ (0.7\mathrm{nm})]_N$ that when the Co thickness is optimized to $x \approx 3$ nm and the number of repeat optimized to $N \approx 20$, the magnetic domain pattern present in the material at remanence can undergo a full transition from a stripe state to a lattice of bubble domains where the density of domain is drastically increased by a factor 10 or more [11-13]. To best characterize and control these morphological transitions, one needs to well visualize the magnetic domain patterns in the film at the nanoscale. [12,14] With spatial resolution down to $\approx$ 20-25 nm, magnetic force microscopy (MFM) is a common way to image nanoscale magnetic domain patterns in thin ferromagnetic films with PMA. However, the scanning nature of MFM often requires limiting the size of the image, typically in the range of 1 - 20 μm and finding a tradeoff between the scanning duration and spatial resolution. When quantifying physical features such as average domain size and domain density, finite size effects may significantly affect statistical estimates, especially when magnetic domains get massively cut at the edge of the image. Because the characterization of magnetic states and morphological magnetic transitions heavily rely on the accuracy of such estimates, it crucial to correctly account for any existing finite image size effect.

Methods

To address the finite size effect question, we study here three MFM images with distinctive domain patterns: stripe, bubble and mixed patterns. These patterns were observed in [Co (3 nm) /Pt (0.7 nm)]$_N$ multilayers exhibiting PMA, where the Co thickness of 3 nm and the number of repeat N had been optimized to maximize domain densities, based on our previous studies [13,14]. The bubble and stripe patterns were achieved in the same material, for which N = 20, by applying an out-of-plane magnetic field of different magnitudes: 4 kOe for the stripe pattern and 6 kOe for the bubble pattern. The mixed state was obtained on a sample with N = 18 by bringing the material to remanence after applying a field of 7 kOe. The MFM images were collected with an in-situ field on a Nanoscope V Dimension 3100 instrument. To obtain reliable statistical results, large images up to 40 x 40 μm^2 for the stripe pattern and 20 x 20 μm^2 for the bubble and mixed patterns were collected. For the stripe, bubble, and mixed patterns, the scan rates were 0.254 Hz, 0.509 Hz, and 0.500 Hz per line, respectively. The spatial resolution, defined here by the pixel size was 9.8 nm (40 μm / 4096 pixels), 19.5 nm (20 μm / 1024 pixels), and 39 nm (20 μm / 512 pixels), respectively. These large images were binarized, partitioned into square blocks, and statistics were computed over all the blocks.

To estimate domain densities and domain sizes, the MFM images were binarized using MATLAB. We designed an algorithm that uses a binarize function [15] with adaptive thresholding [16] based on Gaussian statistics followed by morphological line erosion and disk opening. The binarization was optimized on the sensitivity, neighborhood size, morphological line length and line angle, and morphological disk radius parameters. The 2D correlation [17] was maximized using the Pattern Search optimizer [18]. The correlation values achieved in the stripe, bubble, and mixed pattern were 0.906, 0.855, and 0.799 respectively. This demonstrates sufficiently good binarization for the given resolutions. The resulting binarized images represent local magnetization where white and black respectively correspond to aligned and reversed magnetization direction with respect to the applied out-of-plane magnetic field. The binarized images were then partitioned into square blocks of length L, with L successively taking the values of 20, 10, 5, 2.5 and 1.25 μm.

Once the binarization completed, we extracted domain properties by using the MATLAB's Region Property function [19] with the number of connected regions and area of these regions being the output properties for white and black domains, respectively. The domain density of a given color was estimated by dividing the total number of domains of that color by the block area and rescaling the result per $100\ \mu m^2$. This operation was carried on each individual block, The individual densities were averaged over all the blocks, for a given L. The density plots show these average domain densities along with their standard deviation, as a function of L. Domain area distributions (averaged over all the blocks) are also shown for each given L. In the presented histograms, the bin size is 0.01 μm^2 for the stripe pattern and $0.001\ \mu m^2$ for the bubble and mixed patterns. The average area plots show the average domain area , along with its standard deviation, for each given L. These averages excluded outliers. The interpolation for the comparative density plots was carried by using a pchip algorithm.

Results

Results for a predominant stripe pattern are displayed in Fig.1. The close-up view in Fig.1a taken from a 40 x 40 μm^2 MFM image shows a domain pattern mostly made of aligned stripes with sparse forks and a few trapped bubbles. The extracted densities, plotted in Fig.1b, show the same trend for the reverse (white) and aligned (black) domains. Starting from the smallest partition size L, the domain density ρ rapidly drops to eventually plateau when L increases. For the reversed (white) domains, the average density ρ_w decreases from ~ 760 domains/ 100 μm^2 at L = 1.25 μm down to ~ 148 domains/ 100 μm^2 at L = 40 μm. The plateauing value is interpreted as the true density value ρ_w one would measure in the absence of finite scan size effects (infinite image). Likewise, the average density ρ_b for the aligned (black) domains decreases from 525 domains/ 100 μm^2 at L = 1.25 μm down to 3 domains/ 100 μm^2 at L = 40 μm. In this pattern, the presence of forks and bubbles causes $\rho_w > \rho_b$ with the difference $\rho_w - \rho_b$ eventually reaching 145 domains/ 100 μm^2.

The distribution of individual domain areas in Fig.1c, shows a wide spread of areas from 0 to 1 μm^2. Depending on the partition size L, additional peaks appear at random locations on top of the uniform base distribution. From these area distributions, an averaged domain area was extracted in Fig 1d. The average domain area gradually increases when L increases, growing from 0.06 μm^2 at L = 1.25 μm to 0.32 μm^2 at L = 40 μm, a drastic increase by a factor 5.3. This trend is consistent with the density trend, illustrating the effect of the finite scan size, resulting in stripes being artificially ended at the edges of the image.

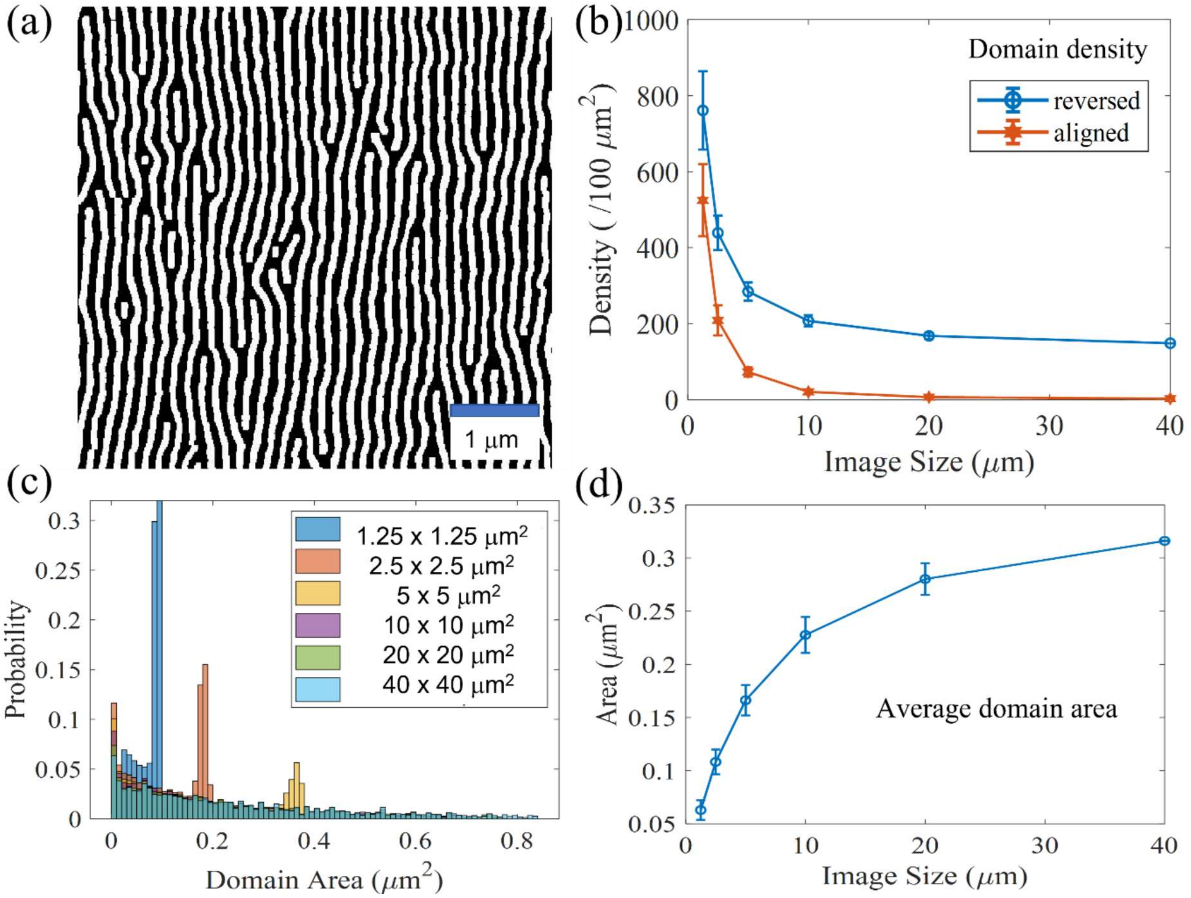

FIG. 1. Results for a predominantly **stripe pattern**. (a) Close-up view from a 40x40 μm^2 MFM image (binarized); (b) Density of white domains ρ_w and black domains ρ_b, as function of the image size it is estimated on; (c) Distribution of domain areas for the reversed (white) domains for various partition sizes *L*. The bin size is 0.01 μm^2; (d) Averaged domain area as function of the image size *L*.

Results for a mixed stripe-bubble pattern are displayed in Fig.2. The close-up view in Fig.2a taken from a 20 x 20 μm^2 MFM image shows a mix of distinct aligned stripes and chains of bubbles. The extracted black and white domain densities, ρ_b and ρ_w, plotted in Fig.2b, show the same trend with *L*. This trend mimics the trend previously observed in the case of stripe pattern, except, in the mixed state, the decrease is not as steep and the difference $\rho_w - \rho_b$ is more pronounced, now reaching 716 domains/ 100 μm^2 at *L* = 20 μm. Also, the plateauing value for ρ_w is much higher, now around 760 domains/ 100 μm^2, while the plateauing value for ρ_b remains relatively low at 45 domains/ 100 μm^2.

The distributions of white domain areas, in Fig.2c, shows a nearly Gaussian distribution that peaks at 0.0065 μm^2 for all the partition sizes *L*. We attribute this peak to the large number of bubble domains. The peak area of 0.0065 μm^2 corresponds to an average bubble radius of 45 nm (bubble diameter 90 nm), consistent with earlier findings for N=18 [13]. From these area distributions, an average domain area, averaged over all (bubble and stripe) domains, was extracted and plotted in Fig 2d. The average domain area gradually increases when *L* increases, growing from 0.031 μm^2 at *L* = 1.25 μm to 0.047 μm^2 at *L* = 40 μm. This 52% increase is relatively moderate compared to the extent of the distributions, with standard deviations as large as $\pm 0.013\ \mu m^2$. Consistent with the density trend, this increase in average domain area is essentially due to the artificial shortening of the stripes being cut at the edge of the image. However, the consistent peak position in the area distribution indicates that the average bubble size is not affected by the image size *L* (as long as *L* is larger than the bubble size, a condition that is largely satisfied here).

Results for a predominant bubble pattern are displayed in Fig.3. The close-up view in Fig.3a taken from a 20 x 20 μm^2 MFM image shows a lattice of bubbles. The extracted densities, ρ_b and ρ_w, plotted in Fig.3b, show the same trend, where the domain density ρ decreases and eventually plateau when *L* increases. This trend mimics the trend previously observed in the case of stripe and mixed pattern, except, in the bubble state, the difference $\rho_w - \rho_b$ is even more pronounced, reaching up to 1898 domains/ 100 μm^2 at *L* = 20 μm, with plateauing values of 1907 domains/ 100 μm^2 for ρ_w and only 9 domains/ 100 μm^2 for ρ_b. This large discrepancy between white and black densities reflects the predominance of white bubble over a black background.

The distribution of individual domain areas, in Fig.3c, peaks at ~ 0.012 μm^2 for all the partition sizes *L*. The peak area of 0.012 μm^2 corresponds to an average bubble radius of 62 nm (bubble diameter 124 nm), consistent with earlier findings for *N* = 20 [13]. The area distribution is narrower compared to the stripe and mixed patterns, with a standard deviation smaller than $\pm 0.003\ \mu m^2$ in the case of the bubble pattern. Also, the average value is much closer to the peak value, indicating that most domains are bubbles of similar size. The extracted average domain area, averaged over all domains, is plotted in Fig 3d. The average domain area slightly increases when *L* increases, growing from 0.017 μm^2 at *L* = 1.25 μm to 0.022 μm^2 at *L* = 20 μm. This 28 % increase is much smaller compared to the case of stripe patterns, due to a smaller proportion of long stripes in the bubble pattern, resulting in limited cutting effects at the edge of the image.

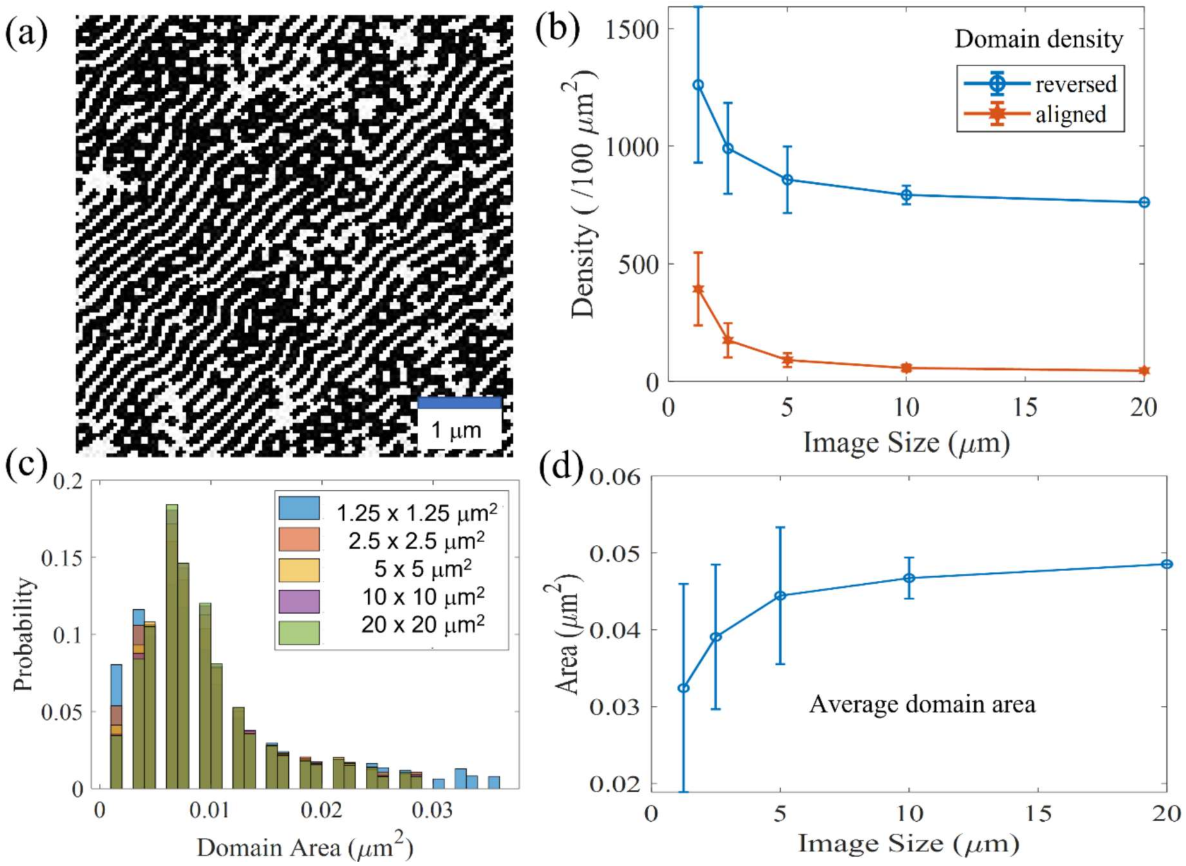

FIG. 2. Results for a **mixed stripe-bubble pattern**. (a) Close-up view from a 20 x 20 μm^2 MFM image (binarized); (b) Density of white domains ρ_w and black domains ρ_b, as function of the image size it is estimated on; (c) Distribution of domain areas for the reversed (white) domains for various partition sizes *L*. The bin size is 0.001 μm^2; (d) Averaged domain area as function of the image size *L*.

Discussion

Our data shows consistent finite scan size effects and suggests that the extent of these effects may depend on the morphology of the domain patterns. To compare the extent of the finite scan size effects in the various morphologies, we plotted in Fig.4 the density ρ_w for the stripe, mixed and bubble patterns against each other. The absolute density plot in Fig.4a illustrates the gradual increase in density when evolving from stripes to bubbles, with the asymptotic density ρ_w increasing from 148 domains/ 100 μm^2 in the stripe case, to 761 domains/ 100 μm^2 in the mixed case, and to 1898 domains/ 100 μm^2 in the bubble case. Comparing these densities once normalized to their asymptotic value, in Fig.4b, shows that the finite scan size effect is however much weaker for the bubble pattern compared to the stripe pattern. As summarized in Table 1, the overestimation (artificial excess) in density $\Delta\rho$ caused by finite scan size only reaches 28% for the bubble pattern compared to 412% for the stripe pattern when L = 1.25 μm.

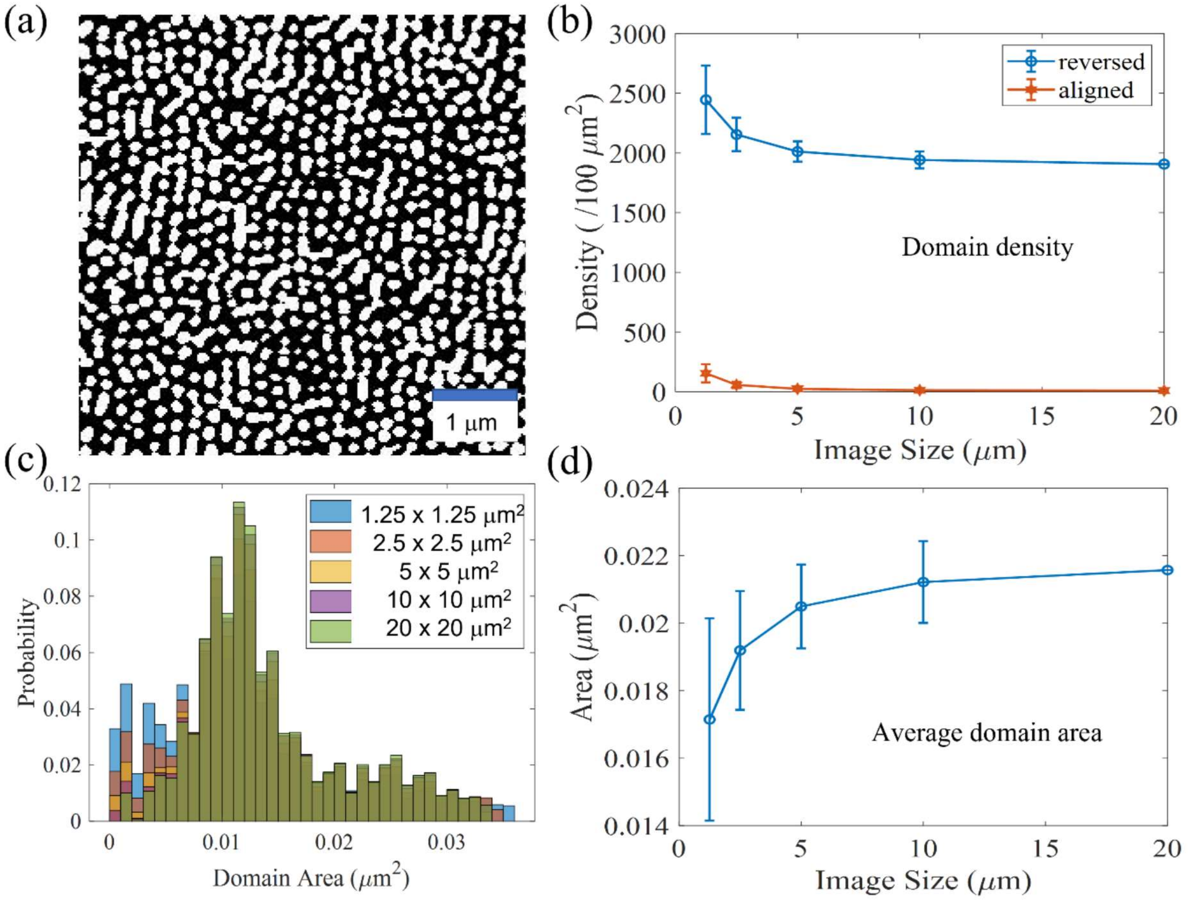

FIG. 3. Results for a predominantly **bubble pattern**. (a) Close-up view from a 20 x 20 μm^2 MFM image (binarized); (b) Density of white domains ρ_w and black domains ρ_b, as function of the image size it is estimated on; (c) Distribution of domain areas for the reversed (white) domains for various partition sizes *L*. The bin size is 0.001 μm^2; (d) Averaged domain area as function of the image size *L*.

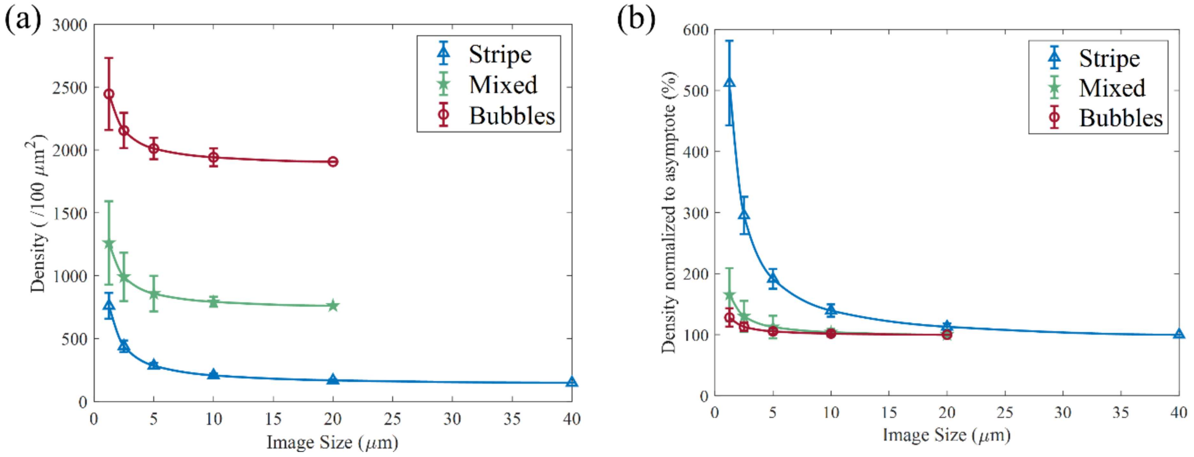

FIG. 4. Comparative plots for the stripe, mixed and bubble states. (a) Density ρ_w of reversed domains as function of the image size it is estimated on, with interpolated curves; (b) Same density curves, normalized to their asymptotic value for comparison purposes.

From this data, we extracted, in Table 1, cutoff minimum image sizes using various criteria, based on limiting the excess density $\Delta\rho$ to 10% or to 1 %. Using the 1% criterion, the data suggests that the minimum image size to obtain reliable accurate statistics for our bubble patterns is around 13 x 13 μm^2. With bubble sizes in the range of 100-120 nm, and distance between bubbles around 250 nm, this corresponds to about 2500 bubbles per image or ~ 50 bubbles in any direction if assuming a regular hexagonal lattice of bubbles. For the stripe pattern, the 1% criterion leads to a minimum image size of around 35 x 35 μm^2. With the stripe width matching the bubble diameter of ~100-125 nm and a black-white stripe period in the range of 200-250 nm, it corresponds to about 140 aligned stripes (of same color) per image.

	Excess density $\Delta\rho$ (%) at various *L*				*Cutoff (minimum) image size (μm)*	
Morphology	10 μm	5 μm	2.5 μm	1.25 μm	$\Delta\rho < 10$ %	$\Delta\rho < 1$ %
Bubbles	1.8%	5.5%	13%	28%	3.2	12.9
Mixed	4.1%	13%	30%	66%	6.2	15.6
Stripes	39%	91%	195%	412%	23	35

Table 1. Selected values for the excess density and cutoff image sizes for the various morphologies: bubble, mixed and stripe states, where the bubble diameter and stripe width are both around 100 nm. The excess density $\Delta\rho$, here listed for various image sizes *L*, is normalized to the asymptotic density value and provided in %, (also see Fig. 4b). The cutoff image size is estimated using various criteria: the normalized excess density $\Delta\rho < 10$ % and 1 %.

Additionally, the data suggests that neither the scanning rate nor the pixel size affect the domain density estimate, as long as the Nyquist sampling criterion is satisfied, i.e., there are enough pixels per domain. If the pixel size is too big with respect to domain size, the Nyquist criterion may not be satisfied for all domains, producing poor quality image and affecting the accuracy of the binarization process, and affecting the estimation of domain densities and domain average size. Here, the Nyquist criterion is largely satisfied for all the presented images, with pixel sizes smaller than 40 nm and down to 10 nm, and domain sizes larger than 100 nm, giving a minimum of 5 pixels and up 100 pixels to define each individual bubble domain. With the Nyquist criterion being satisfied, the data suggests that the domain density and average domain size are not affected by the pixel size, but mainly by the total image size.

Conclusion

Our study shows that when imaging magnetic domain patterns, the finite size of the image can significantly affect the quantitative characterization of magnetic states and associated magnetic transitions. We conducted our study on thin Co/Pt multilayers with perpendicular magnetic anisotropy, exhibiting magnetic domain patterns of various shapes, from stripes to bubbles, depending on the applied magnetic field history. We found that the scan rate and pixel size did not affect our statistics, as long as the pixel size remains small enough to satisfy the Nyquist sampling criterion. However, we found that to obtain reliable statistical estimates of quantities such as domain densities and average domain sizes, the image size needs to be large enough, and even larger for stripes patterns compared to bubble patterns. We estimated cutoff minimum sizes based on the density excess relative to asymptotic values. If limiting the excess density to 1%, we found that in the case of a bubble pattern, the image needs to include at least about 2500 bubbles, or about 50 bubbles in any direction when in a close packed lattice of bubbles. For 100 nm bubbles, this would translate into minimum image size of about 10 x 10 μm^2. In the case of a stripe pattern, the image needs to include at least about 100 aligned stripes of same color, using that same criterion. For 100 nm wide stripes (200 nm period), this translates into 20 x 20 μm^2 minimum image size. If the image size is smaller than these suggested cutoff sizes, one should account for finite size effects, resulting in a significant underestimation of the domain size and overestimation of the domain density which may end up being several 100 % off.

Acknowledgment

We thank the group of Prof. Olav Hellwig from TU Chemnitz and HZDR in Germany, for sample supply. This research was supported by the NSF REU award #2051129 and the College of Mathematical & Physical Sciences at Brigham Young University.

References

[1] J. L. Archer, L. Tocci, P. K. George, and T. T. Chen, IEEE Trans. Magnetics **8**, 695-700 (1972).
[2] A. H. Eschenfelder, *Magnetic Bubble Technology Vol. 14* (Springer Berlin, 1980).
[3] J. Davies, R. Clover, B. Lieberman, and D. Rose, IEEE Trans. Magn. **16**, 1106 (1980).
[4] R. Allenspach, M. Stampanoni, and A. Bischof, Phys. Rev. Lett. **65**, 3344 (1990).
[5] N. Ogawa, W. Koshibae, A. J. Beekman, N. Nagaosa, M. Kubota, M. Kawasaki, and Y. Tokura, PNAS **112**, 8977 (2015).
[6] V. Gehanno, Y. Samson, A. Marty, B. Gilles, and A. Chamberod, J. Magn. Magn. Mater. **172**, 26-40 (1997)
[7] O. Hellwig, A. Berger, and E. E. Fullerton, Phys. Rev. Lett. **91**, 197203 (2003).
[8] J. E. Davies, O. Hellwig, E. E. Fullerton, G. Denbeaux, J. B. Kortright, and K. Liu, Phys. Rev. B **70**, 224434 (2004).
[9] K. Chesnel, E.E. Fullerton, M.J. Carey, J.B. Kortright, S.D. Kevan, Phys. Rev. B **78** (13), 132409 (2008)
[10] K. Chesnel, A. Safsten, M. Rytting, E.E. Fullerton, Nature Comm. **7**, 11648 (2016)
[11] A.S. Westover, K. Chesnel, K. Hatch, P. Salter, O. Hellwig, J. Magn. Magn. Mater. **399**, 164-169 (2016)
[12] K. Chesnel, A.S. Westover, C. Richards, B. Newbold, M. Healey, L. Hindman, *et al.*, Phys. Rev. B **98** (22), 224404 (2018)
[13] L. Fallarino, A. Oelschlägel, J.A. Arregi, A. Bashkatov, F. Samad, B. Böhm, *et al.*, Phys. Rev. B **99** (2), 024431 (2019)
[14] A. Gentillon, C. Richards, L.A. Ortiz-Flores, J. Metzner, D. Montealegre, *et al.*, AIP Advances **11** (1), 015339 (2021)
[15] “Binarize 2-D Grayscale Image or 3-D Volume by Thresholding - MATLAB Imbinarize.” n.d. Www.mathworks.com. https://www.mathworks.com/help/images/ref/imbinarize.html.
[16] “Adaptive Image Threshold Using Local First-Order Statistics - MATLAB Adaptthresh.” n.d. Www.mathworks.com. Accessed November 8, 2022. https://www.mathworks.com/help/images/ref/adaptthresh.html.
[17] “2-D Correlation Coefficient - MATLAB Corr2.” n.d. Www.mathworks.com. https://www.mathworks.com/help/images/ref/corr2.html.
[18] “Find Minimum of Function Using Pattern Search - MATLAB Patternsearch.” n.d. Www.mathworks.com. Accessed November 8, 2022. https://www.mathworks.com/help/gads/patternsearch.html.
[19] “Measure Properties of Image Regions - MATLAB Regionprops.” n.d. Www.mathworks.com. https://www.mathworks.com/help/images/ref/regionprops.html.

Bibliography

[1] H. Van den Berg, R. Coehoorn, M. Gijs, P. Grünberg, T. Rasing, and K. Röll, *Magnetic multilayers and giant magnetoresistance: fundamentals and industrial applications* (Springer Science & Business Media, 2013), Vol. 37.

[2] R. Wood, "Future hard disk drive systems," Journal of Magnetism and Magnetic Materials **321,** 555–561 (2009), current Perspectives: Perpendicular Recording.

[3] J. Grollier, D. Querlioz, and M. D. Stiles, "Spintronic Nanodevices for Bioinspired Computing," Proceedings of the IEEE **104,** 2024–2039 (2016).

[4] M. T. Johnson, P. J. H. Bloemen, F. J. A. d. Broeder, and J. J. d. Vries, "Magnetic anisotropy in metallic multilayers," Reports on Progress in Physics **59,** 1409–1458 (1996).

[5] K. Chesnel *et al.*, "Morphological stripe-bubble transition in remanent magnetic domain patterns of Co/Pt multilayer films and its dependence on Co thickness," Physical Review B **98,** 224404 (2018), pRB.

[6] A. S. Westover, K. Chesnel, K. Hatch, P. Salter, and O. Hellwig, "Enhancement of magnetic domain topologies in Co/Pt thin films by fine tuning the magnetic field path throughout the hysteresis loop," Journal of Magnetism and Magnetic Materials **399,** 164–169 (2016).

[7] L. Fallarino, A. Oelschlägel, J. A. Arregi, A. Bashkatov, F. Samad, B. Böhm, K. Chesnel, and O. Hellwig, “Control of domain structure and magnetization reversal in thick Co/Pt multilayers,” Physical Review B **99,** 024431 (2019), pRB.

[8] https://www.nanosurf.com/en/support/afm-modes overview, “AFM Modes Overview,”, 2022.

[9] https://blog.brukerafmprobes.com/guide-to-spm-and-afm-modes/magnetic-force-microscopy mfm/, “Magnetic Force Microscopy - MFM,”, 2011.

[10] M. C.-K. C. Michael M. Vaka, Joey Ray, “Finite image size effects on the characterization of magnetic domain patterns via magnetic force microscopy,” (2022).

Index